UiT The Arctic University of Norway

Faculty of Science and Technology
Department of Physics and Technology

A new Method for Estimating 3-Dimensional Ionospheric Currents from Ground-Based Magnetometers

Erik Thom

FYS-3931 Master's thesis in Space Physics 30SP … July 2022

Abstract

The ionosphere is a region of the upper atmosphere where a significant rate of photo-ionisation from solar ultraviolet radiation cause an increased plasma density. In this region a system of electrical currents flow, driven by electric fields generated by fluctuating dynamics within the Earths magnetosphere. These fluctuating dynamics are caused by interactions between the magnetosphere and the solar wind and interplanetary magnetic field. The ionospheric current flow causes disturbances in the Earths geomagnetic field called substorms, which have been measured by ground based magnetometers for over 100 years. Different techniques have been developed to determine the ionospheric currents from these measurements, to get a better understanding of the magnetosphere-ionosphere coupling. In this thesis we will investigate what current distributions can be resolved with a large and dense network of ground based magnetometers. With this in mind a new method to estimate ionospheric currents on a simple wireframe model from ground-based magnetic field observations based of general linear inverse methods is presented. The method is based on a Tikhonov type regularization modified to include Kirchoff's current law to regularize the solution in a physically sensible way. The method is tested on a set of artificial current systems to see how well it performs.

Contents

List of Figures

1 Introduction

This thesis presents a general method to estimate ionosheric currents from ground based measurements of magnetic field variations.

1.1 Motivation

As a current system in the ionosphere develops due to solar wind activity and ionosphere-magnetosphere dynamic coupling, magnetic fields are generated leading to a disturbance on Earth's magnetic field (Brekke, 2012). These disturbances are observable at ground level and can lead to significant effects on infrastructure, e.g. induce DC currents in power-line grids or disturb directional drilling. During substorms with strong auroral-electrojets these induced currents can lead to failing power-transformers and power outages like in Quebec 1989 (Allen et al., 1989). In a society dependent on continuous elctricity supply, such occurances should be prevented, therefore a good understanding of the solar wind and the magnetosphere-ionosphere dynamic coupling is needed. One way of doing this is by estimating the ionospheric current system through measurements of the magnetic field disturbances from magnetic observatories and magnetometers.

Several methods have been developed to achieve this, with the Spherical Elementary Current System (SECS) (Amm, 1997) being a widely used model today. A problem with this model is that it can only estimate horizontal equivalent

currents from ground based magnetometer data, as it follows Fukushima's Theorem (Fukushima, 1976), eliminating field aligned currents (FACs) from the estimate. Magnetic field measurements from satellites in low-earth orbit can be used to extend this method to combine the horizontal SECS-currents with the in-situ FAC measurement along the satellite path, but these have limits in how many observations can be made and when and where they can measure data due to a limited amount of satellites following orbital paths.

As Fukushima's theorem has strict conditions that does not necessarily hold in the real world, a new method will be introduced in this thesis that does not rely on this theorem that attempts to estimate the 3-dimensional ionosheric current system from ground based magnetometers only.

1.2 Thesis Structure

Chapter 2 covers the theoretical background of the physics behind ionosheric currents and how these currents can be estimated from magnetic field measurements. Section 2.1 lays out a general understanding of how the sun affects the Earth's atmosphere and magnetosphere through solar radiation and solar wind, and how this in turn leads to electromagnetic processes which causes a system of electric fields and currents to occur in the upper atmosphere. Section 2.2 covers how these current systems generate magnetic fields that can be measured, and how these measurement in turn can be used to estimate the current systems.

Note: Some of the material in chapter 2 is similar to an earlier project paper on a similar topic. This might mark the thesis as plagiarised so this note is placed in case the thesis needs to go through a plagiarism control.

Chapter 3 details a new general method of estimating ionospheric currents from ground based magnetic field measurements. Section 3.1 explains Fukushima's theorem and discusses how the conditions of the theorem does not hold for the actual physics of the real ionosphere-magnetosphere system. Section 3.2 define the setup of a wireframe grid model that we use to model ionospheric currents in 3 dimensions. Section 3.3 covers how the new method uses linear inverse techniques and regularization to estimate the ionosheric currents in the grid model from ground based magnetic field measurements. Section 3.4 explains how the model is tested by trying to estimate a set of artificial current systems for a varying number of measurement stations and comparing the estimated results with the actual current systems.

Chapter 4 shows the results from testing the new estimation method and discusses the performance of the new method.

Chapter 5 summarizes the thesis work and discusses future work.

2

Background

2.1 The physics of ionospheric currents

2.1.1 The solar wind and its interactions with Earth

The most important ways that the Sun affects the Earth are through solar radiation and the solar wind. Solar radiation is the electromagnetic radiation emitted from the sun, with large parts of the ultraviolet (UV) radiation being absorbed in the Earths uppermost atmosphere. Most importantly is the extreme ultraviolet radiation (EUV) where the photons have enough energy to cause photo-ionisation in a region of the upper atmosphere named the thermosphere, sustaining the plasma density in this region creating the ionosphere (e.g. Brekke, 2012). In addition to this electromagnetic radiation the sun continually ejects charged particles, called the solar wind, from its outermost layer. This solar wind carries with it magnetic fields, collectively called the interplanetary magnetic field (IMF). The solar wind and the IMF interacts with the Earths magnetic field and changes its shape and dynamics. The properties of both UV solar radiation and solar wind are dependent on the solar activity, which is correlated with the frequency of e.g. sunspots and coronal mass ejections, all following the solar cycle that has a period of aproximately 11 years. It has been found that this cycle corresponds to a polarity reversal of the Sun's magnetic field, and that the peaks of this cycle has a strong connection to an increased disturbance of the Earths magnetic field.

2.1.2 The magnetosphere

The magnetosphere is the region around Earth where the Earths magnetic field dominates over the IMF (Brekke, 2012). The typical large scale structure is sketched in figure 2.1. Before reaching the magnetosphere, the solar wind first forms a bow shock where it gets slowed down from supersonic to subsonic speeds due to the pressure experienced from the magnetosphere. Afterwards the solar wind reaches the magnetosphere boundary called the magnetopause, where the Earths magnetic field prevent the charged particles from getting closer to the Earth, deflecting the protons toward the evening-side (out of the page) and electrons toward the morning-side (into the page) creating the dayside magnetopause current. The solar wind pressure at this boundary shapes the magnetosphere, compressing the sunward side while stretching out the anti-sunward side, creating a tail called the magnetotail where a magnetotail current flows through the central plasma-sheet (out of the page) and then around the magnetotail lobes (into the page) in the plasma mantle region. However, the interactions between the solar wind and the magnetosphere is not constant, as fluctuating solar activity leads to varying speed, density, and IMF structure within the solar wind. Therefore the rate of solar wind charged particles entering the magnetosphere varies, through magnetic reconnection between the Earths magnetic field lines and the IMF.

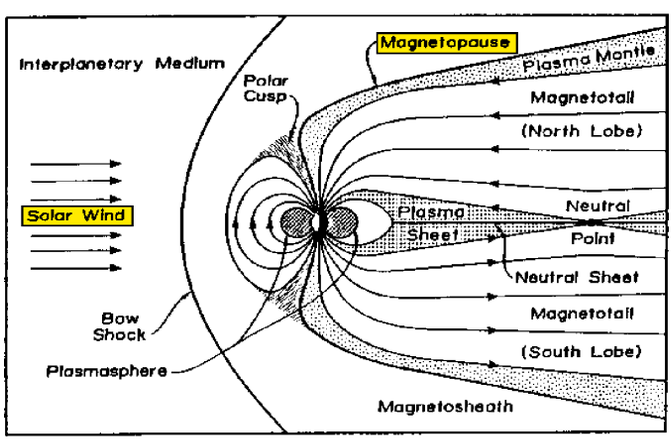

Figure 2.1: A simple diagram of a slice of the Earth's magnetosphere. From Elfritz (2014)

Magnetic reconnection is a process in which magnetic field lines of opposing directions gets pushed together by sufficient pressure forces,leading to the field lines "breaking" and then "reconnecting" to eachother. Figure 2.2 shows the two stages before and after a magnetic reconnection. Though there have been extensive research about the microphysical processess occuring within magnetic reconnection (e.g. Hesse and Cassak, 2020), the typical processes in the reconnection region between the magnetosphere and the IMF is still a

topic of active research as it is a turbulent and difficult region to measure by spacecrafts.

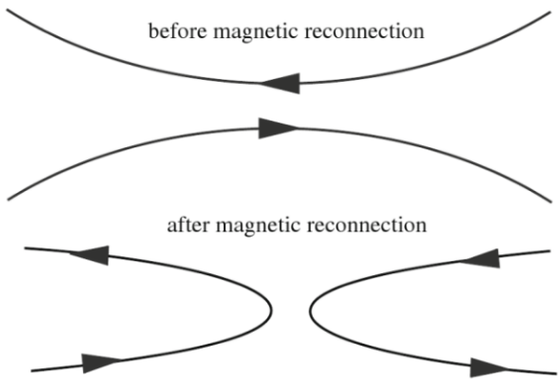

Figure 2.2: A diagram of the two stages before and after a magnetic reconnection. From Wang (2015)

As the IMF of the solar wind have fluctuating structures, magnetic reconnection occurs at varying rates and at different locations of the magnetopause. In the case of a southward oriented IMF there is a high reconnection rate at the sunward side of the Earth. The Dungey cycle (Dungey, 1961) describes the general chain of events occuring for this case, shown in figure 2.3. First the IMF opens the dayside magnetosphere through reconnection (step 1), and then the solar wind pulls the interconnected IMF-magnetosphere field lines to the nightside into the magnetotail (steps 2 and 3). These open field lines are later closed via magnetic reconnection within the magnetotail (step 4). The reconnection creates two separate field lines, moving in opposite directions towards and away from the Earth (steps 5 and 6) with the earthbound field line wrapping around the Earth to the dayside (step 7). The case of a northward oriented IMF usually have a weaker effect on the magnetosphere. However, magnetic reconnection does happen with the magnetotail field lines at the polar regions.

Due to the difference in the magnetic reconnection rates at the magnetopause and within the magnetotail energy is stored in the magnetotail, when the dayside reconnection rate is larger, and released when there is an abrupt large reconnection in the magnetotail. The release of energy accelerates charged particles along magnetic field lines into the ionosphere at the polar regions. This process is called a substorm cycle and has a strong connection to auroral activity, explained briefly in section 2.1.3.

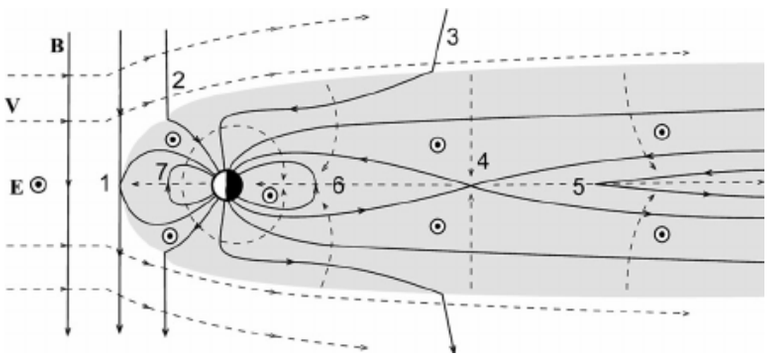

Figure 2.3: A diagram of the Dungey cycle from the opening of the dayside field lines (step 1) to the magnetotail reconnection (step 4) and the replenish of the dayside closed field line (step 7). From Seki et al. (2015)

2.1.3 The ionosphere

The ionosphere is the region in the upper atmosphere, at altitudes of around 60-1000km (Schunk and Nagy, 2009), that contains a significant density of ionized plasma. Figure 2.4 shows the general electron density structure of the ionosphere. As can be seen, the plasma density varies both with the solar cycle and time of day. This shows the significant effects solar radiation has on the ionosphere through photo-ionisation, a process where high energy photons impact neutral atoms and molecules and seperate an electron and produce electron-ion pairs. The plasma is lost through the process of recombination, leading to a plasma density decrease during the night when there is no solar radiation to drive photo-ionisation. The efficiency of the ionisation and recombination processes are different at various altitudes due to changing neutral (atmospheric) and ion compositions and the penetration depths of the EUV-radiation. The uppermost region above 150km with the maximum plasma density, due to a low recombination rate, is called the F region. Below this is a region with a higher rate of recombination, but also a higher ionisation rate at 90-150km which is called the E region. The lowest region at 60-90km is called the D region, with the lowest plasma density in the ionosphere (Richmond, 2007). Electrical currents flow horizontally mainly in the E-region, where collisions start to affect the ion-mobility, due to electromagnetic effects from the IMF-magnetosphere interactions.

Currents in the ionospheric polar cap

The Dungey cycle described in section 2.1.2, is an important part in driving the currents within the ionosphere. The open field lines connecting the IMF to the Earths magnetic field **B** are being pulled across the polar cap by the convection

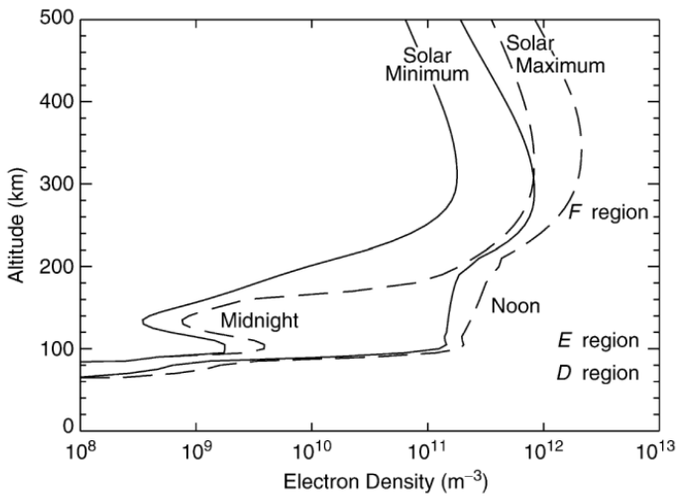

Figure 2.4: Electron density structure of the ionosphere at 18°N, 67°W during the September equinox at noon and midnight for solar minimum(solid lines) and maximum (dashed lines). From Richmond (2007)

electric field generated by the solar wind plasma travelling at a velocity $\mathbf{v}_s$. As the magnetic field lines are assumed pointing vertically downward (upward) in the norhern (southern) polar cap and the solar wind are travelling in the anti-sunward direction, a perpendicular electric field $\mathbf{E}$ is generated going from dawn to dusk across the polar cap (Vasyliūnas, 2012):

$$\mathbf{E} = -\mathbf{v}_s \times \mathbf{B} \tag{2.1}$$

This electric field penetrates into the ionosphere, since the magnetic field lines are near perfect conductors, setting the ionosheric plasma into motion. This motion generates a Pedersen current going from dawn to dusk across the polar cap, while at lower altitudes, a secondary Hall current is also generated due to a higher rate of ion-neutral collisions, going across the polar cap in the sunward direction. These currents are then closed either totally within the ionosphere or through currents along the magnetic field lines, called field aligned currents (FAC), to be closed in the magnetosphere. A schematic of the polar cap currents is shown in figure 2.7. Integrating over the height of the ionosphere, the ionospheric current density can be described by

$$\mathbf{J} = \int_{ion} \mathbf{j} dz = \Sigma_P \mathbf{E}'_\perp - \Sigma_H \frac{\mathbf{E}'_\perp \times \mathbf{B}}{B} + \Sigma_\parallel \mathbf{E}'_\parallel \tag{2.2}$$

where $\mathbf{B}$ is the magnetic field, $\mathbf{E}' = \mathbf{E}'_\perp + \mathbf{E}'_\parallel$ is the electric field in an Earth-fixed frame of reference and Σ_P, Σ_H and $\Sigma_\parallel$ are the height-integrated Pedersen, Hall and parallel conductivites respectively. The subscripts $\perp$ and $\parallel$ denote, respectively, perpendicular and parallel to the magnetic field. The height dependent Pedersen (σ_P) and Hall (σ_H) conductivites are both highly dependent

on ionospheric plasma density and neutral composition, while the parallel conductivity ($\sigma_{\parallel}$) becomes very large at altitudes over 100km (Richmond, 2007). The altitude profile of the conductivites can be seen in figure 2.5, while a model of the height-integrated Pedersen conductivity can be seen in figure 2.6.

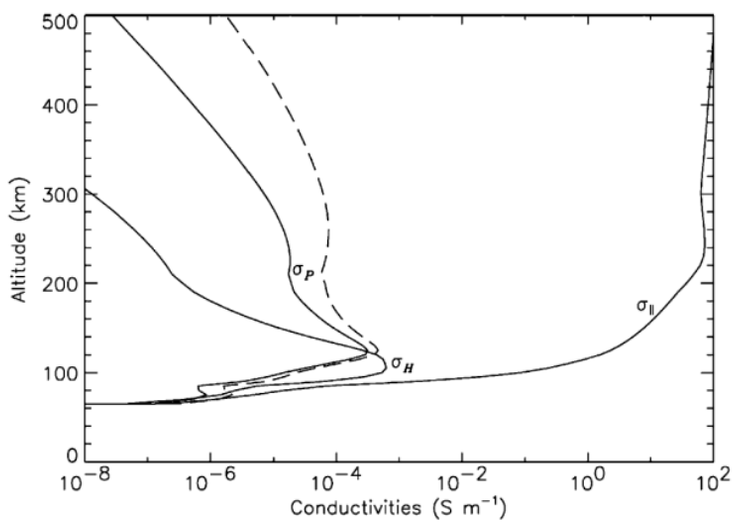

Figure 2.5: Solid lines: Height profiles of the Pedersen σ_P, Hall σ_H and parallel $\sigma_{\parallel}$ conductivites at 18°N, 67°W during the September equinox. Dashed line: Pedersen conductivity at solar maximum. From Richmond (2007).

The auroral-electrojet and substorms

Current activity in the ionosheric region around the polar cap, called the auroral oval, are driven by the magnetic reconnection within the magnetotail. From the reconnection a closed magnetic field line is created towards the Earth. This field line will get pulled sunward, accelerating charged particles from the plasma sheet along magnetic field lines towards the Earth. These particles precipitate into the ionosphere, exciting and ionising neutrals within the auroral oval. The excited particles then release energy as electromagnetic radiation known as the auroral display, while the ionised particles significantly change the height integrated Hall and Pedersen conductivities (e.g. Robinson et al., 1987), as illustrated in figure 2.6. The closed field-lines continue to drift sunward past the Earth to replenish the dayside magnetic field. The field lines convect sunward across the dawn and dusk flanks of the polar cap, generating an electric field (eq. (2.1)) as plasma drift sunward together with the field lines. This electric field penetrates into the ionosphere within the auroral oval, pointing in the dusk to dawn direction. This drives a Pedersen current across the auroral zone in the dusk to dawn direction, and a secondary Hall current along the auroral oval in the anti-sunward direction. The Hall currents are called eastward and

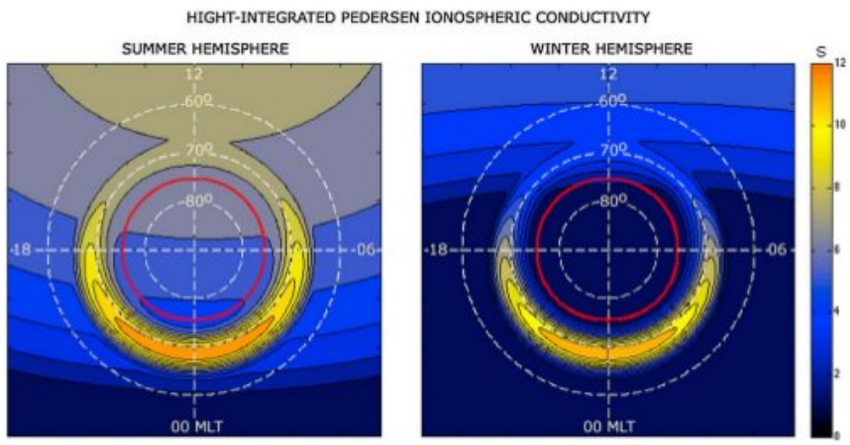

Figure 2.6: Model of height-integrated Pedersen conductivity in the ionosphere for the summer (left) and winter (right) hemispheres. The conductivity scale is in Siemens, with low conductivity shown as blue and higher conductivity shown as yellow and orange. The red circles indicate the polar cap boundaries. Sun exposure increases the conductivity, as seen with the difference between the two hemispheres, while the auroral zones contains an enhanced conductivity from accelerated auroral electrons. From W. Lyatsky (2015).

westward auroral-electrojets, as shown in figure 2.7, and they create large disturbances of the Earths geomagnetic field called substorms.

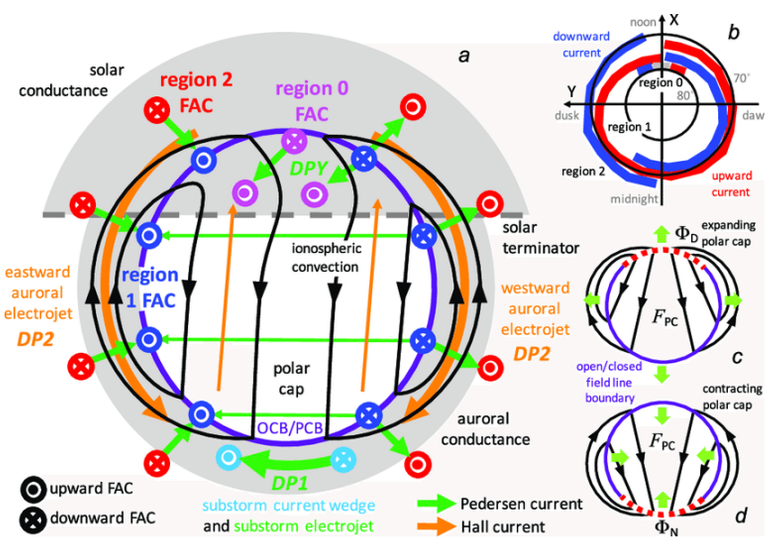

Figure 2.7: A schematic of the ionospheric current systems (in color) and convection (in black) at the norhern polar cap. Noon and midnight is at the top and bottom of the figure respectively. From Milan et al. (2017)

2.2 Estimating ionospheric currents from magnetic field measurements

Charges in motion (i.e. currents) generate a magnetic field. The magnetic field generated can be calculated by the Biot-Savart law

$$\mathbf{B}(\mathbf{r}) = \frac{\mu_0}{4\pi} \iiint_V \frac{(\mathbf{J}dV) \times \mathbf{r}'}{|\mathbf{r}'|^3} \tag{2.3}$$

where $\mathbf{B}$ is the magnetic field at position $\mathbf{r}$ generated from a current density $\mathbf{J}$ flowing through a volume V and $\mathbf{r}'$ is the displacement vector between $\mathbf{r}$ and the volume element dV. If the current can be approximated as running through an infinitely thin wire, eq. (2.3) can be modified to

$$\mathbf{B}(\mathbf{r}) = \frac{\mu_0}{4\pi} \int_C \frac{(I\, d\mathbf{l}) \times \mathbf{r}'}{|\mathbf{r}'|^3} \tag{2.4}$$

where the current I flows along a curve C, $d\mathbf{l}$ is a vector element along the curve path and $\mathbf{r}'$ is the displacement vector between $\mathbf{r}$ and $d\mathbf{l}$. The current I can be moved outside the integral if it is assumed constant and uniform, e.g. for a discrete section of an ionospheric current traveling along a short distance C_i at a given point in time,

$$\mathbf{B}(\mathbf{r}) = \frac{\mu_0}{4\pi} I_i \int_{C_i} \frac{d\mathbf{l} \times \mathbf{r}'}{|\mathbf{r}'|^3} \tag{2.5}$$

This shows that $\mathbf{B}(\mathbf{r})$ depends linearly on the current I_i. This makes it possible to describe the observed $\mathbf{B}(\mathbf{r}_s)$ as a set of linear equations of the type

$$\mathbf{B}(\mathbf{r}_s) = \sum_i \mathbf{T}_{s,i} I_i \tag{2.6}$$

where

$$\mathbf{T}_{s,i} = \frac{\mu_0}{4\pi} \int_{C_i} \frac{d\mathbf{l} \times \mathbf{r}'_s}{|\mathbf{r}'_s|^3} \tag{2.7}$$

This set of linear equations makes it possible to estimate the ionospheric currents from magnetic field measurements at various ground locations $\mathbf{r}_s$ through a linear inverse problem, further explained in section 3.3.

3

A new method of estimating ionospheric currents

In this thesis we will investigate what current distributions can be resolved with a large and dense network of ground based magnetometers. With this in mind a new method to estimate ionospheric currents on a simple wireframe model from ground-based magnetic field observations based of general linear inverse methods is presented. The method is based on a Tikhonov type regularization modified to include Kirchoff's current law to regularize the solution in a physically sensible way.

3.1 Fukushima's Theorem

One tool that has been widely used to simplify the the ionospheric current estimation problem is Fukushima's theorem. It makes it possible to constrain the problem to only the horizontal ionospheric currents. The theorem states that beneath the ionosphere the magnetic fields generated from FACs and horizontal circularly symmetric diverging currents cancel eachother out. Therefore ground based magnetic field measurements cant distinguish the two. The theorem has been used to model the ionospheric currents with divergence-free current

systems. One method to estimate ionospheric currents from ground based magnetometer data is the SECS-method developed by Amm (1997), Amm and Viljanen (1999).

Fukushima's theorem only holds as long as two key conditions are valid;

1. Ionospheric conductance is spatially constant

2. FACs are perpendicular to the ground

As most works using Fukushima's theorem mention the assumption of constant conductance does not easily hold (e.g. Newell and Gjerloev, 2014). Therefore some models, like SECS, ignore assumptions about conductance and electric field by decomposing the ionospheric current system into a divergence-free system and curl-free system (Amm, 1997, Untiedt and Baumjohann, 1993). The second assumption made about perpendicular FACs only holds strong where the Earth's magnetic field is close to vertical. As a large amount of ionospheric research is done within the northern auroral region, this assumption has mostly been accepted (e.g. Laundal et al., 2015).

In the ionosphere the currents into and out of the E-region are not vertical, but flows along the Earth's magnetic field. Here we will show that for such cases Fukushima's theorem does not hold in a mathematical sense. That Fukushima's theorem strictly holds only for a vertical current diverging into horizontal currents can be easily seen if we look at a vertical downward current and an equally strong upward FAC with diverging and converging horizontal currents that cancel eachother out (figure 3.1). As (a) in figure 3.1 generates zero magnetic field below the horizontal currents according to Fukushima's theorem, the magnetic field generated from (b) has to equal the magnetic field generated from (c). Therefore as the direction of the FAC changes with increasing inclination from the vertical, the geometry of the magnetic field from the FAC will deviate from the geometry of the magnetic field from the vertical current in (c) such that more of the magnetic field generated from (b) is detectable below the horizontal currents.

To quantitavely test this a downward vertical current and a downward FAC following the IGRF model (Alken et al., 2021), intersecting at 100km above the ground, is compared at $(20°lat, 20°long)$ and $(70°lat, 20°long)$ (figure 3.2). A set of 50 measurement locations are placed with a Gaussian random distribution at ground level within 5° co-latitude and longitude range from the intersection point to measure the generated magnetic field according to the Biot-Savart law. The magnetic field measurements are compared in the radial, co-latitudinal and longitudinal directions for each station to show how much the magnetic field structure changes (figures 3.3 and 3.4).

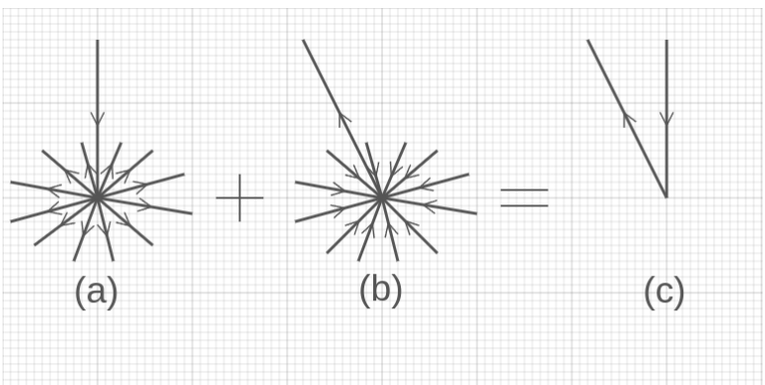

Figure 3.1: A downward vertical current with diverging horizontal currents (a) and an equally strong upward FAC with converging horizontal currents (b) added together such that the horizontal currents cancel leaving only the vertical current and FAC (c).

As can be seen in figures 3.3 and 3.4 the magnetic measurement data from the FAC system does deviate from the vertical current system. As expected the magnetic field deviation is greatest close to the equator where the magnetic field curves into a horizontal direction while there is a smaller deviation in the auroral region where the magnetic field are closer to vertical. This deviation shows that ground magnetomers should be able to measure magnetic fields generated from FACs to a certain degree in opposition to Fukushima's theorem.

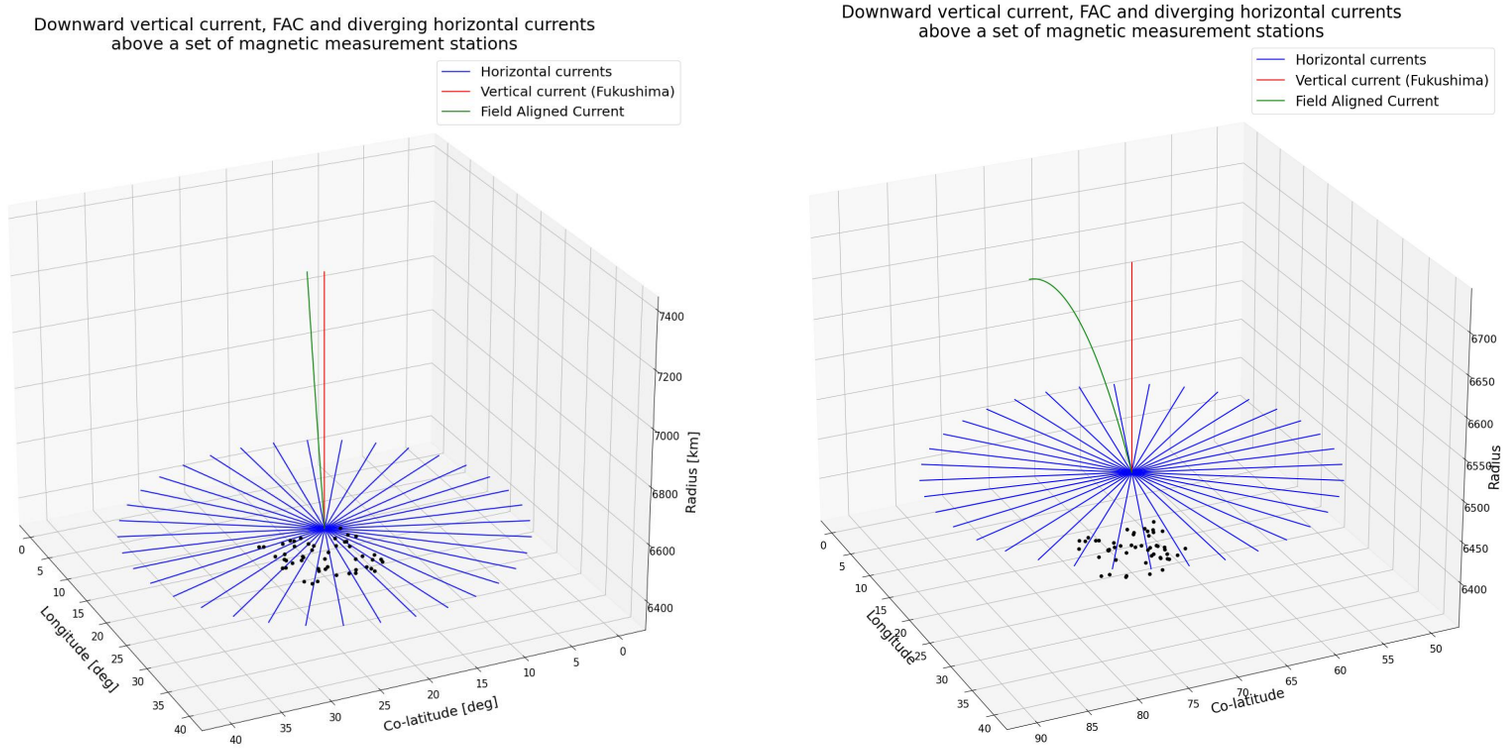

Figure 3.2: A system of a 10kA vertical current and an equally strong FAC travelling downward to the same point at 100km above the ground at (20°co-lat., 20°long.) (left) and (70°co-lat., 20°long.) (right). From the intersection point the 10kA diverges out along horizontal currents. On the ground is 50 magnetic measurement stations spread out with a Gaussian random distribution within 5° co-latitude and longitude range from the intersection point.

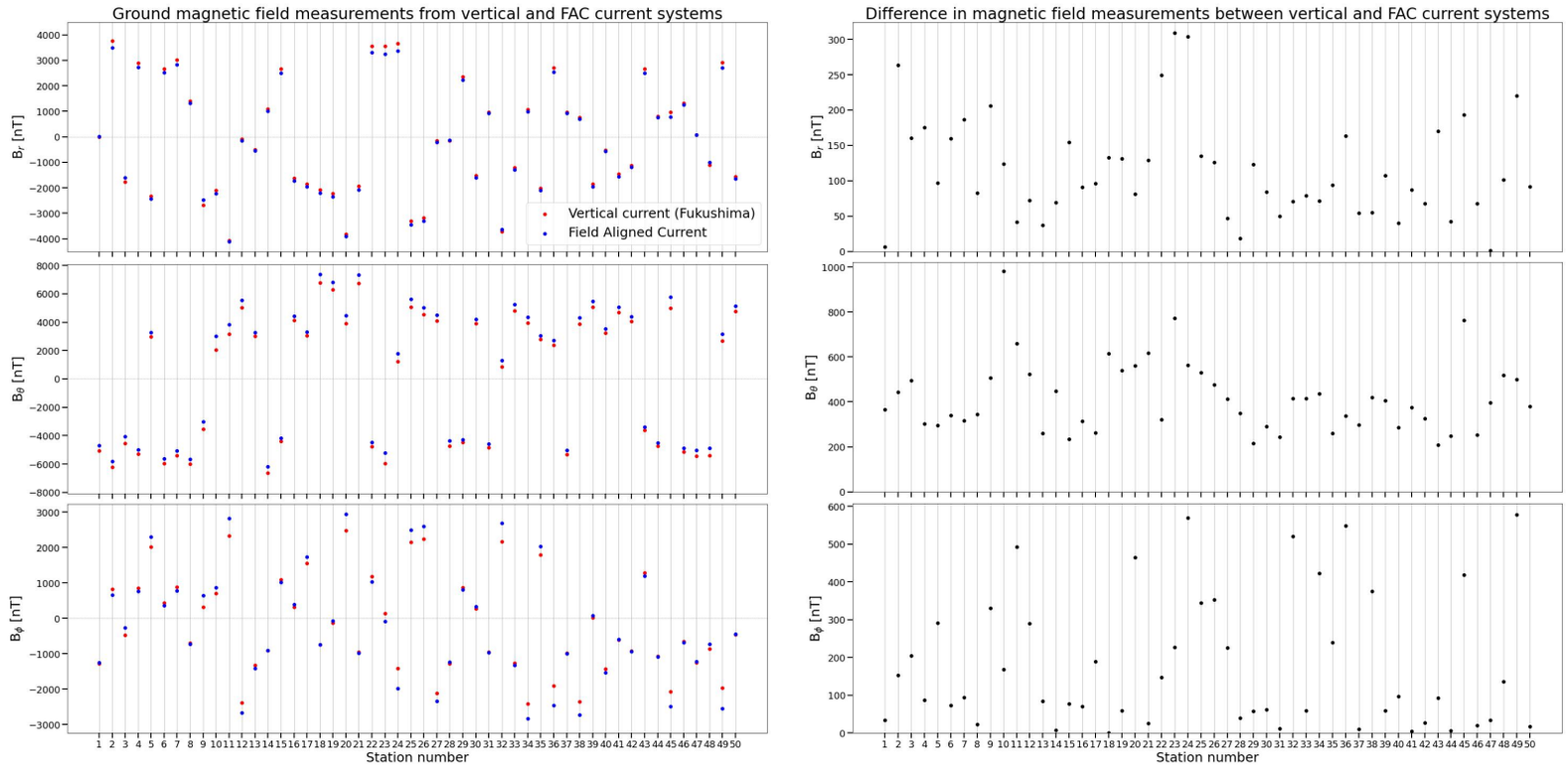

Figure 3.3: The magnetic field measured by the 50 stations in the left system in figure 3.2 in radial (top), colatitudinal (center) and longitudinal (bottom) directions. The right figure show the measurements from the two current systems (vertical current + horizontal) and (FAC + horizontal), while the left figure show the difference between the two current systems.

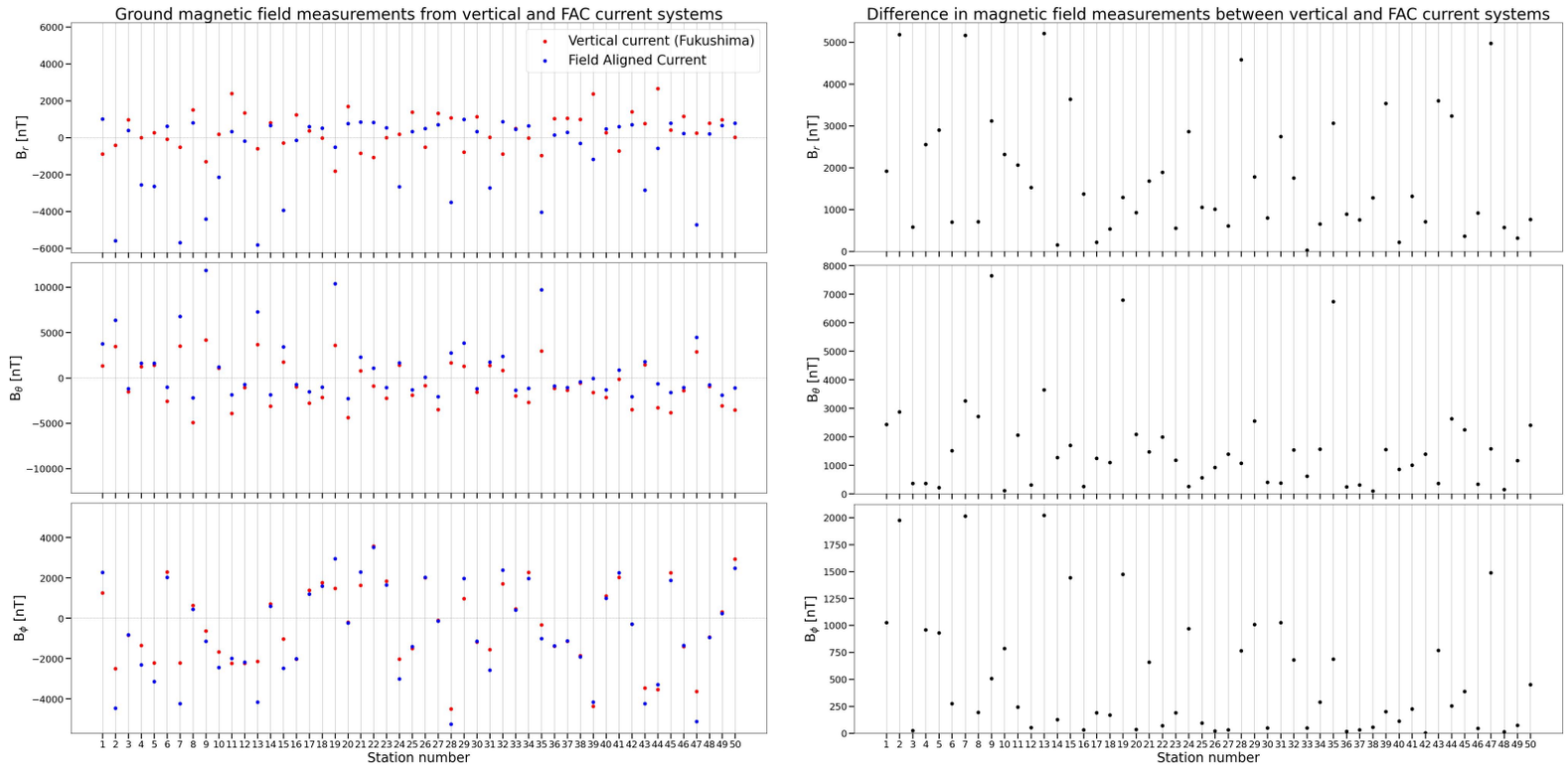

Figure 3.4: The magnetic field measured by the 50 stations in the right system in figure 3.2 in radial (top), colatitudinal (center) and longitudinal (bottom) directions. The right figure show the measurements from the two current systems (vertical current + horizontal) and (FAC + horizontal), while the left figure show the difference between the two current systems.

3.2 Ionospheric grid system

For our estimation method a new simple wireframe grid model is developed called "Grid of Ionospheric Currents in 3D" (GICi3D). The model consists of a 2-dimensional grid of location points in spherical coordinates (r, θ, ϕ), corresponding to radial, co-latitude and longitude coordinates. Each point contains a current vector $\mathbf{I} = (I_r, I_\theta, I_\phi)$ (figure 3.5). The radial part of the current vector I_r describes the FAC moving along the International Geomagnetic Reference Field (IGRF) (Alken et al., 2021) between the grid point and a given r_{max}, while the horizontal parts I_θ, I_ϕ describes the currents to the south of, and east of the grid point respectively. A positive value describes a current going out from the grid point, while a negative value describes a current going towards the grid point.

Figure 3.6 shows how a horizontal current going from one location (θ_0, ϕ_0) to another location (θ_N, ϕ_M) is represented in this model. The current is distributed into fractions in the (θ, ϕ) directions onto all points within the local grid $((\theta_0, \phi_0) - (\theta_N, \phi_M))$. For each point (θ_n, ϕ_m) within this local grid, where $0 \leq n < N$ and $0 \leq m < M$, the current is calculated as

$$I_{\theta_n} = I_{in} \cdot \frac{N - n}{(N - n) + (M - m)} \tag{3.1}$$

$$I_{\phi_m} = I_{in} \cdot \frac{M - m}{(N - n) + (M - m)} \tag{3.2}$$

where I_{in} is the total current going into the point (θ_n, ϕ_m). The total horizontal current system within the model is then the sum of all these local current grids. This means that currents in arbitrary directions will have a horizontal width of a certain amount of grid cells as shown in figure 3.7 which shows the vector field representation of the green current in figure 3.6.

3.3 Estimating ionospheric currents using linear inverse problem techniques

As described in section 2.2 the ionospheric currents in this model, represented as constant currents flowing along uniform infinitely thin wires, generate magnetic fields at various measurement locations described by the Biot-Savart law (eq. (2.5)). These magnetic fields can be measured by ground magnetometer stations, along with other disturbances to the Earths magnetic field but those are ignored as its outside the scope of this project. As shown in eq. (2.6), the measured magnetic field and the currents in the GICi3D model can be

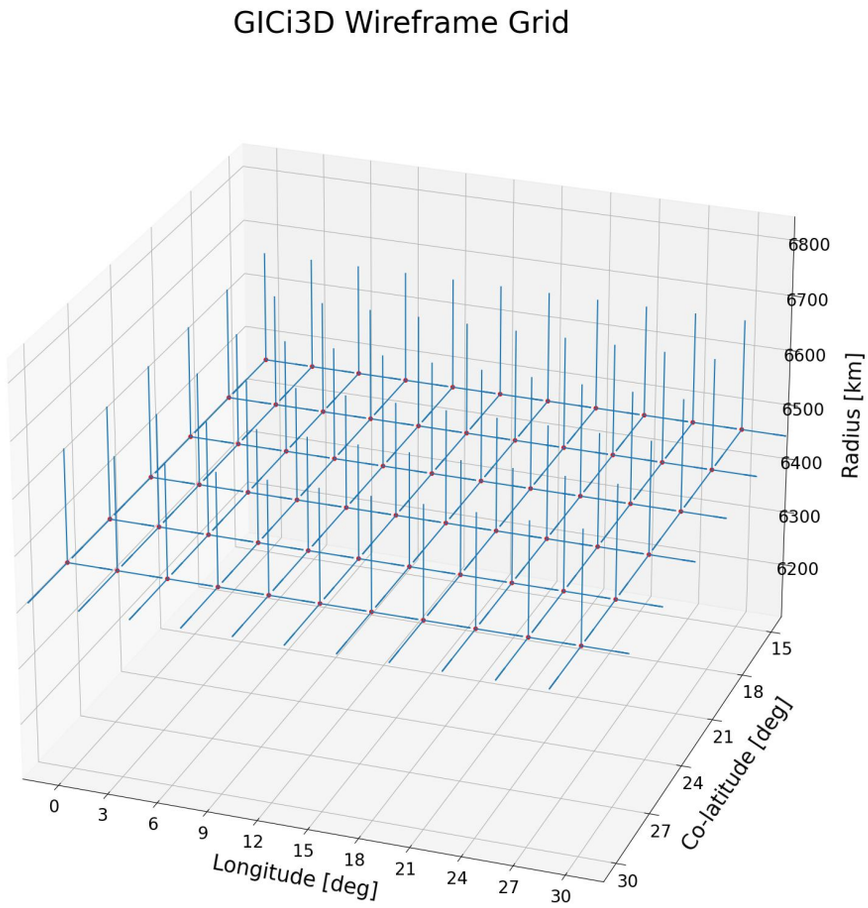

Figure 3.5: An example of the GICi3D wireframe grid model. A 2 dimensional grid of location points (red dots) who contain a current vector in the three spherical directions $\mathbf{I} = (I_r, I_\theta, I_\phi)$ (blue lines) representing the currents above, to the east of and to the south of the location point.

represented as a set of linear equation

$$\mathbf{B} = \underline{\underline{\mathbf{T}}} \cdot \mathbf{I} \tag{3.3}$$

where

$$\mathbf{B} = [B_r(\mathbf{r}_{1,obs}),\ B_\theta(\mathbf{r}_{1,obs}),\ B_\phi(\mathbf{r}_{1,obs}), \ldots,\ B_r(\mathbf{r}_{K,obs}),\ B_\theta(\mathbf{r}_{K,obs}),\ B_\phi(\mathbf{r}_{K,obs})]^T \tag{3.4}$$

is the magnetic field observations at the ground positions $\mathbf{r}_{k,obs} = (R_E, \theta_{k,obs}, \phi_{k,obs})$, $k = 1, ..., K$ with R_E being the radius of the Earth,

$$\mathbf{I} = [I_r(\mathbf{r}_{1,grid}),\ I_\theta(\mathbf{r}_{1,grid}),\ I_\phi(\mathbf{r}_{1,grid}), \ldots,\ I_r(\mathbf{r}_{L,grid}),\ I_\theta(\mathbf{r}_{L,grid}),\ I_\phi(\mathbf{r}_{L,grid})]^T \tag{3.5}$$

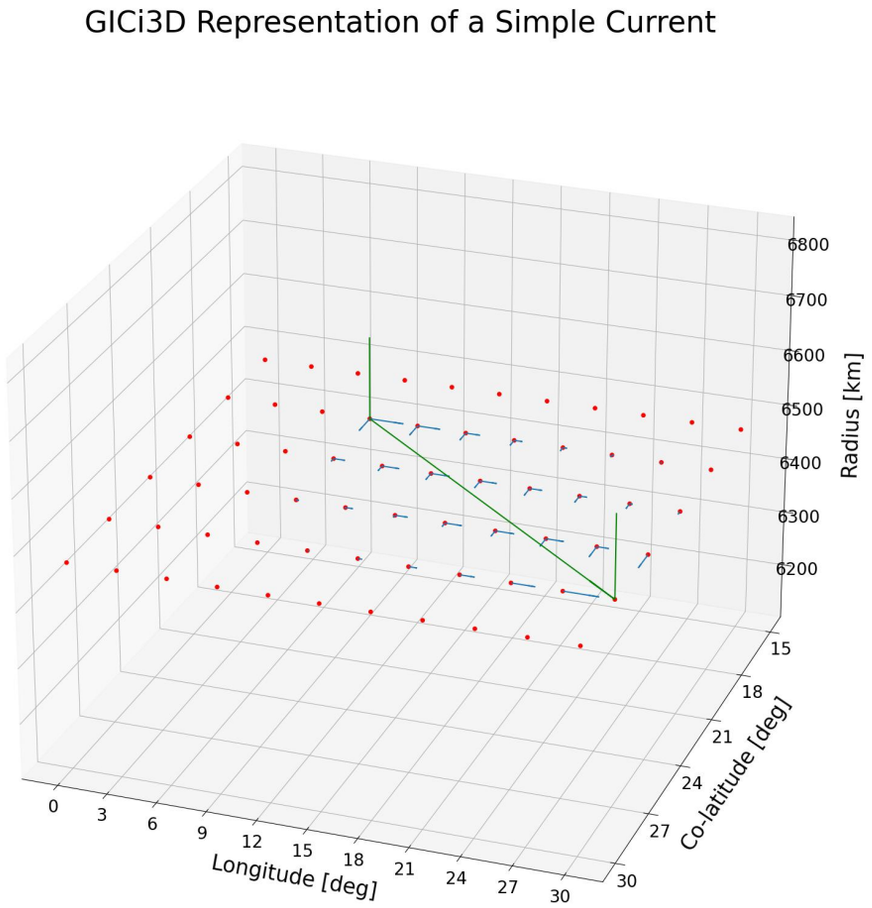

Figure 3.6: An example of how a horizontal current in any arbitrary direction (green line) is represented in the GICi3D model. The current is distributed along the co-latitudinal and longitudinal directions over the surrounding grid points (blue lines)

is the currents at grid points $\mathbf{r}_{l,grid} = (R_I, \theta_{l,grid}, \phi_{l,grid}),\ l = 1, ..., L$ with R_I being the radius of the model grid, and

$$\underline{\underline{\mathbf{T}}} = \begin{bmatrix} T_{1r,1r} & T_{1r,1\theta} & T_{1r,1\phi} & T_{1r,2r} & \dots & T_{1r,L\phi} \\ T_{1\theta,1r} & T_{1\theta,1\theta} & T_{1\theta,1\phi} & T_{1\theta,2r} & \dots & T_{1\theta,L\phi} \\ T_{1\phi,1r} & T_{1\phi,1\theta} & T_{1\phi,1\phi} & T_{1\phi,2r} & \dots & T_{1\phi,L\phi} \\ T_{2r,1r} & T_{2r,1\theta} & T_{2r,1\phi} & T_{2r,2r} & \dots & T_{2r,L\phi} \\ \vdots & \vdots & \vdots & \vdots & & \vdots \\ T_{K\phi,1r} & T_{K\phi,1\theta} & T_{K\phi,1\phi} & T_{K\phi,2r} & \dots & T_{K\phi,L\phi} \end{bmatrix} \tag{3.6}$$

is the magnetic effect between each point $\mathbf{r}_{k,obs}$ and $\mathbf{r}_{l,grid}$ from a current system with a uniform current magnitude of $1A$ across the whole grid.

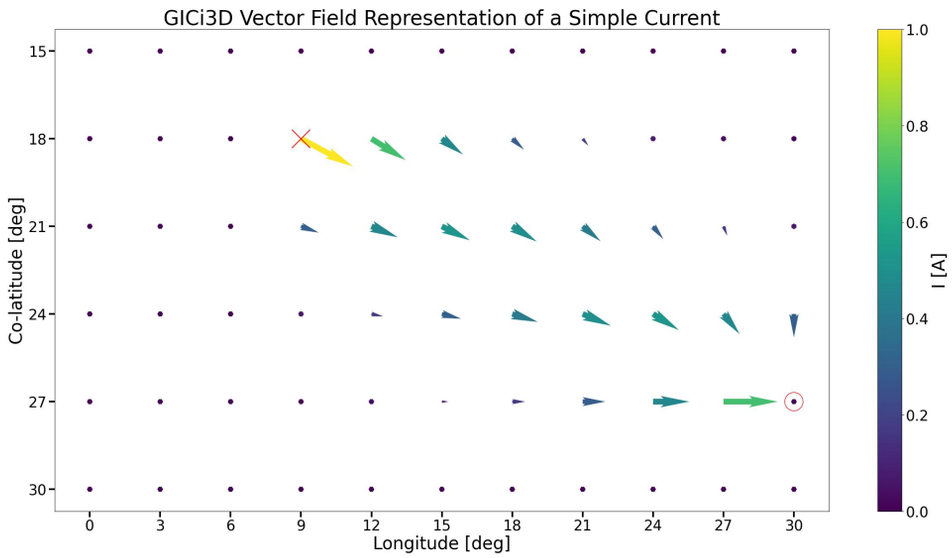

Figure 3.7: An example of how a current in the GICi3D model can be represented as a vector field. This shows a vector field of the green current in figure 3.6.

3.3.1 Solving the inverse linear problem

Eq. (3.3) is to be solved for the ionospheric current distribution $\mathbf{I}$, which is a linear inverse problem that can be solved using a variety of techniques. Since $\underline{\underline{\mathbf{T}}}$ is ill-conditioned and underdetermined due to the number of measurement stations usually being much lower than the number of current elements ($K << L$), a technique regularizing the problem has been used.

A technique called Singular Value Decomposition (SVD) (Aster et al., 2019a) is used with zeroth order Tikhonov regularization (Aster et al., 2019b). SVD decomposes the matrix $\underline{\underline{\mathbf{T}}}$ into

$$\underline{\underline{\mathbf{T}}} = \underline{\underline{\mathbf{U}}}\,\underline{\underline{\mathbf{S}}}\,\underline{\underline{\mathbf{V}}}^T \tag{3.7}$$

where $\underline{\underline{\mathbf{U}}}$ and $\underline{\underline{\mathbf{V}}}^T$ are orthognal matrices containing the basis vectors for the vector space of $\mathbf{B}$ and $\mathbf{I}$ respectively, while $\underline{\underline{\mathbf{S}}}$ is a diagonal matrix containing the singular values of $\underline{\underline{\mathbf{T}}}$. With this the Moore-Penrose pseudo-inverse of $\underline{\underline{\mathbf{T}}}$ can be written as

$$\underline{\underline{\mathbf{T}}}^{\dagger} = \underline{\underline{\mathbf{V}}}\,\underline{\underline{\mathbf{S}}}^{-1}\,\underline{\underline{\mathbf{U}}}^T \tag{3.8}$$

such that eq. (3.3) can be solved as

$$\mathbf{I} = \underline{\underline{\mathbf{V}}}\,\underline{\underline{\mathbf{S}}}^{-1}\,\underline{\underline{\mathbf{U}}}^T\mathbf{B} \tag{3.9}$$

As $\underline{\underline{\mathbf{T}}}$ is underdetermined, $n_{\mathbf{B}} < n_{\mathbf{I}}$, we only have at most $n_{\mathbf{B}}$ nonzero singular values in $\underline{\underline{\mathbf{S}}}$ and since $\underline{\underline{\mathbf{T}}}$ is ill-conditioned the smallest singular values are very

close to zero. This becomes a problem when there is noise η involved in the linear system

$$\mathbf{B} = \underline{\underline{\mathbf{U}}}\ \underline{\underline{\mathbf{S}}}\ \underline{\underline{\mathbf{V}}}^T \mathbf{I} + \eta \tag{3.10}$$

$$\mathbf{I} = \underline{\underline{\mathbf{V}}}\ \underline{\underline{\mathbf{S}}}^{-1}\ \underline{\underline{\mathbf{U}}}^T \mathbf{B} + \underline{\underline{\mathbf{V}}}\ \underline{\underline{\mathbf{S}}}^{-1}\ \underline{\underline{\mathbf{U}}}^T \eta \tag{3.11}$$

because the smaller singular values in the inverse $\underline{\underline{\mathbf{S}}}^{-1}$ becomes very large, or infinite for the case of singular values being zero, which amplifies the noise-components in η. To minimize the effect of these noise-components zeroth order Tikhonov modifies $\underline{\underline{\mathbf{S}}}^{-1}$ with a regularization parameter α such that

$$\frac{1}{s_{ii}} \cdot \frac{s_{ii}^2}{s_{ii}^2 + \alpha^2} \tag{3.12}$$

is used instead of $\frac{1}{s_{ii}}$ where s_{ii} is the singular values in $\underline{\underline{\mathbf{S}}}$. The second factor in eq. (3.12) weights the singular values, such that the larger singular values are left mostly unchanged while the impact of the smaller singular values are damped. It can be shown that this solves

$$\underset{\mathbf{I}}{\operatorname{argmin}}\ (\mathbf{B} - \underline{\underline{\mathbf{T}}}\ \mathbf{I})^T (\mathbf{B} - \underline{\underline{\mathbf{T}}}\ \mathbf{I}) + \alpha \mathbf{I}^T \mathbf{I} \tag{3.13}$$

which is the Tikhonov regularization.

3.3.2 Adding constrain using Kirchoffs current law

Since there are no large-scale accumulation of electrical charges in the ionosphere we know that the divergence of the current is zero everywhere. This becomes Kirchoff's current law for our wireframe model. This can be used to further regularize our problem and minimize error in the solution of the inverse regression. In our model the condition is set that every grid point $\mathbf{r}_{l,grid}$ has to follow Kirchoffs current law such that the sum of currents flowing into the point has to equal the sum of currents flowing out of the point. This can be represented as a linear system of equations

$$0 = \underline{\underline{\mathbf{K}}} \cdot \mathbf{I} \tag{3.14}$$

where $\underline{\underline{\mathbf{K}}}$ is an $L \times 3L$ matrix where each row corresponds to a grid point with 1s and -1s added to the column elements corresponding to outgoing and incoming currents to that point. This can be combined with eq. (3.3) to give

$$\begin{bmatrix} \mathbf{B} \\ 0 \end{bmatrix} = \begin{bmatrix} \underline{\underline{\mathbf{T}}} \\ \underline{\underline{\mathbf{K}}} \end{bmatrix} \cdot \mathbf{I} \tag{3.15}$$

which can be solved in the same way, following section 3.3.1. With this condition the solution of the inverse problem is restricted from adding non-existent point charges to the ionospheric current system estimate, which is physically sensible.

3.4 Testing the method

To test the method a grid is created between 20° and 30° co-latitude, 15° and 30° longitude at 100km height above the ground, with 0.5° horizontal seperation between the grid points and the IGRF field lines reaching up to approx. 200km. Within this grid a set of artificial current systems is set up creating magnetic field data at ground locations under the grid. The data is then used to estimate the current systems using the techniques described in sections 3.3.1 and 3.3.2. The estimated current system is then compared with the actual current system to test how accurate and reliable this model is.

The current systems used for testing are:

1. A single eastward current with FACs at the endpoints, travelling a distance of 0.5°, 1°, 3°, 6°, 9°, 12° and 15°.

2. A single southward current with FACs at the endpoints, travelling a distance of 0.5°, 1°, 2°, 4°, 6°, 8° and 10°.

3. An eastward current stream with FACs at the endpoints.

4. A southward current stream with FACs at the endpoints.

5. A multidirectional system of currents moving along north, south, east and west and along field lines splitting and merging at various grid points.

Systems 1 and 2 is testing the resolution of the estimation, with the 0.5° long current acting as a point source. Systems 3 and 4 tests how good the estimation can estimate larger current streams like eastward electrojets and cowling channels. System 5 is a final test to see if the estimation can handle more complex systems with currents moving in seperate directions, diverging and converging out from and into FACs. The testing is done with 500, 200, 100 and 50 ground measurement locations spread with a Gaussian random distribution under the grid.

The implementation of the model and the testing script can be found in `https://github.com/erikthm/masters-thesis.git`

4

Results

Figures 4.2 to 4.38 show some of the results of the method test described in section 3.4. These results will be discussed in this chapter.

A common result among all the current system estimations, for any amount of ground stations, was that the estimated FACs were generally less accurate than the estimated horizontal currents compared to the actual current systems. All the estimated systems had some level of FAC noise surrounding the current system, with the amplitude of the estimated FACs corresponding to the actual FACs determining if they were able to distinguish themselves from the noise. A loss in both resolution and amplitude accuracy in the estimated FACs also happen for several current systems. What determines if the FACs lose accuracy in resolution or magnitude is unknown as a pattern has not been found with the results in this chapter. It can be argued that it is Fukushima's theorem playing a role, as the model grid is positioned within the auroral region such that the FACs are close to the vertical. This might be indicated by the results for the complex multidirectional current system (figures 4.22, 4.27, 4.32 and 4.37), where the FACs split up into or got merged from symmetrical horizontal currents.

The systems of single currents travelling eastward and southward (figures 4.2 to 4.17) were generally well estimated from 500 ground magnetomers. Something to note is the estimations of the edge to egde travelling currents (figures 4.8 and 4.16) which showed how the method loses estimation accuracy when trying to estimate around an area of no ground magnetometers.

The estimated southward and eastward current streams both show interesting behaviour as seen in figures 4.18, 4.19, 4.20 and 4.21. Both types of current systems generate artifacts for the FACs, with the eastward system generated "blobs" of FACs repeating every 6° in the longitudinal direction while the southward stream generated rings of opposite directed FACs surrounding them. The reason for this is currently not well understood.

Note: In the figure texts of the results an estimated system's mean absolute error is given. This is not the mean absolute error between the actual current system and the estimated system as they are originally. Both systems are first normalized to the range $[0, 1]$ before the estimation error is calculated, as it was decided that a better system structure estimation is preferable over a better magnitude estimation.

4.1 Results for 500 magnetometer stations

In this section visuals will be shown for the single eastward currents travelling 0.5°, 3°, 9° and 15°, the single southward currents travelling 0.5°, 2°, 6° and 10°, the eastward current stream, the southward current stream and the multidirectional system of currents..

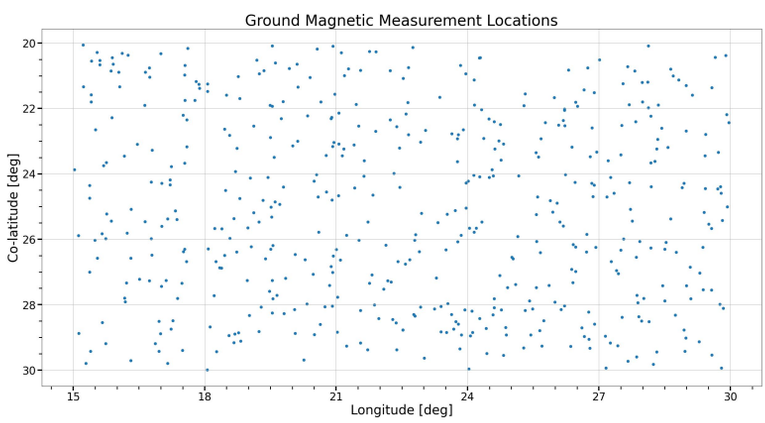

Figure 4.1: 500 randomly distributed ground magnetometer locations within 20° and 30° co-latitude and 15° and 30° longitude.

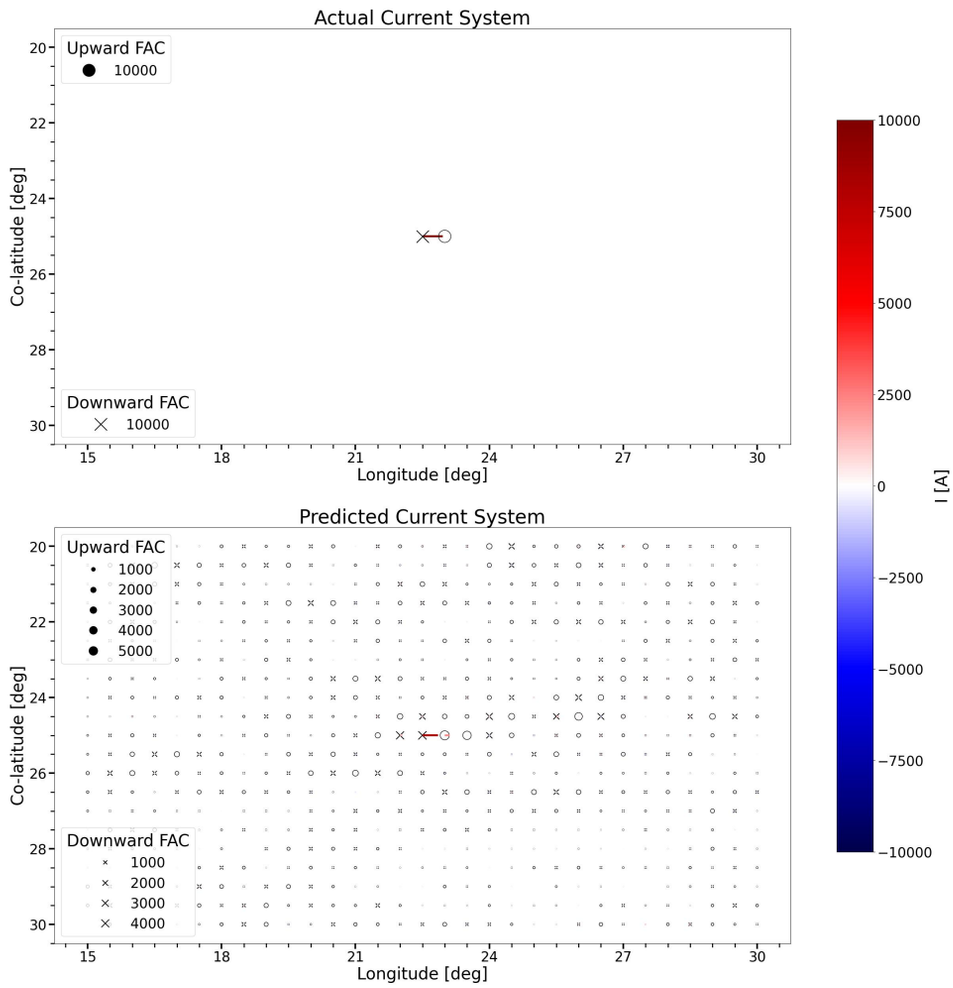

Figure 4.2: Vectorfield of the actual (top) and estimated (bottom) current system of a 10kA downward FAC coming in at (20°co-lat., 22.5°long.) and travelling east 0.5° before travelling as an upward FAC at (20°co-lat., 23°long.). The estimated system manages to estimate the actual current system reasonably well, allthough at a reduced amplitude, but drowning the actual currents in noisy FACs. The estimated system has a mean absolute error of $4.65 \cdot 10^{-2}$.

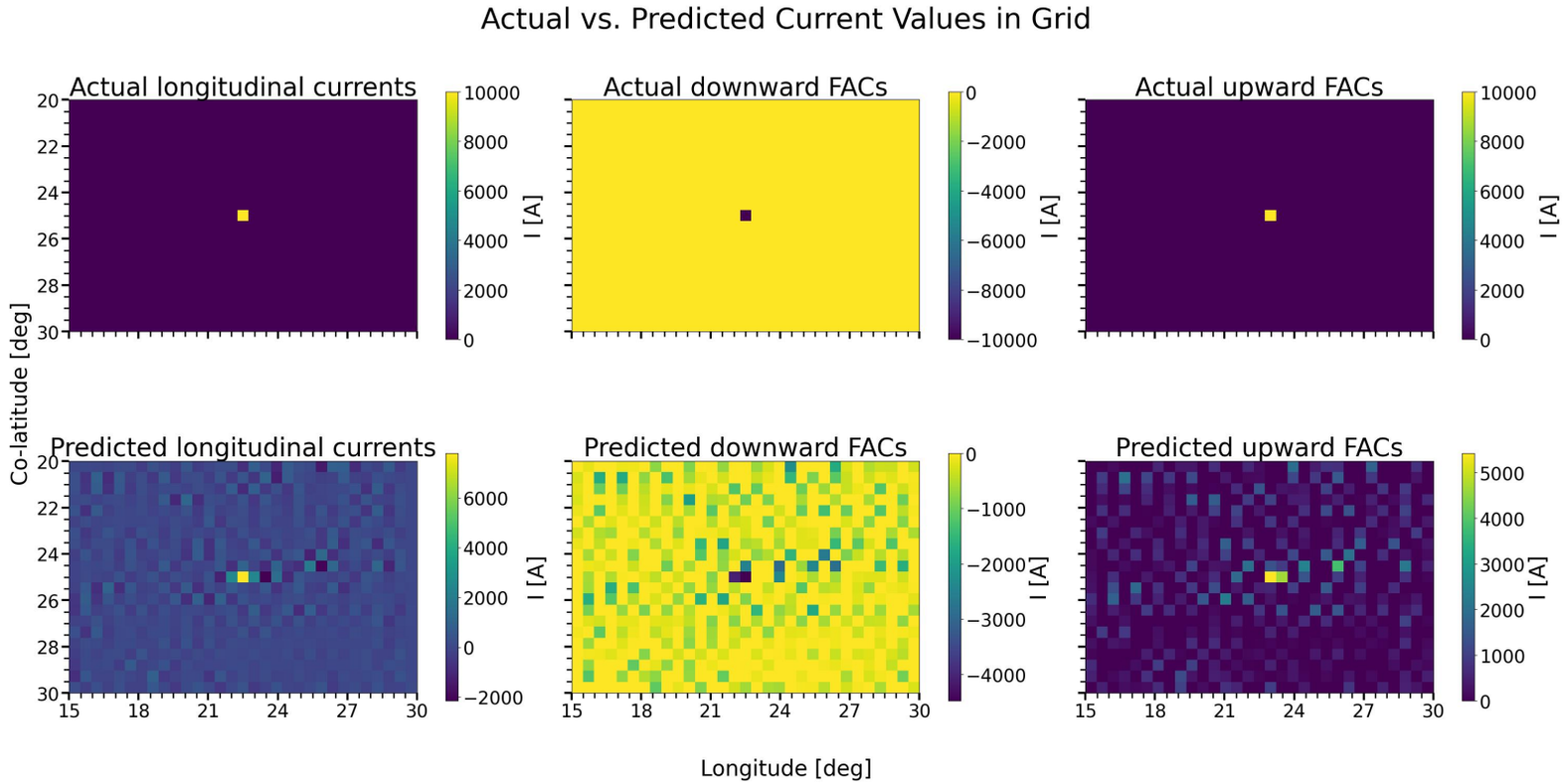

Figure 4.3: The actual (top) and estimated (bottom) longitudinal current (left), downward FAC (center) and upward FAC (right) grid values for a current system of a 10kA downward FAC coming in at (20°co-lat., 22.5°long.) and travelling east 0.5° before travelling as an upward FAC at (20°co-lat., 23°long.). It can be seen that the estimation manages to estimate the longitudinal values generally better than the FAC values, as the estimated FAC values are significantly more noisy than the longitudinal values.

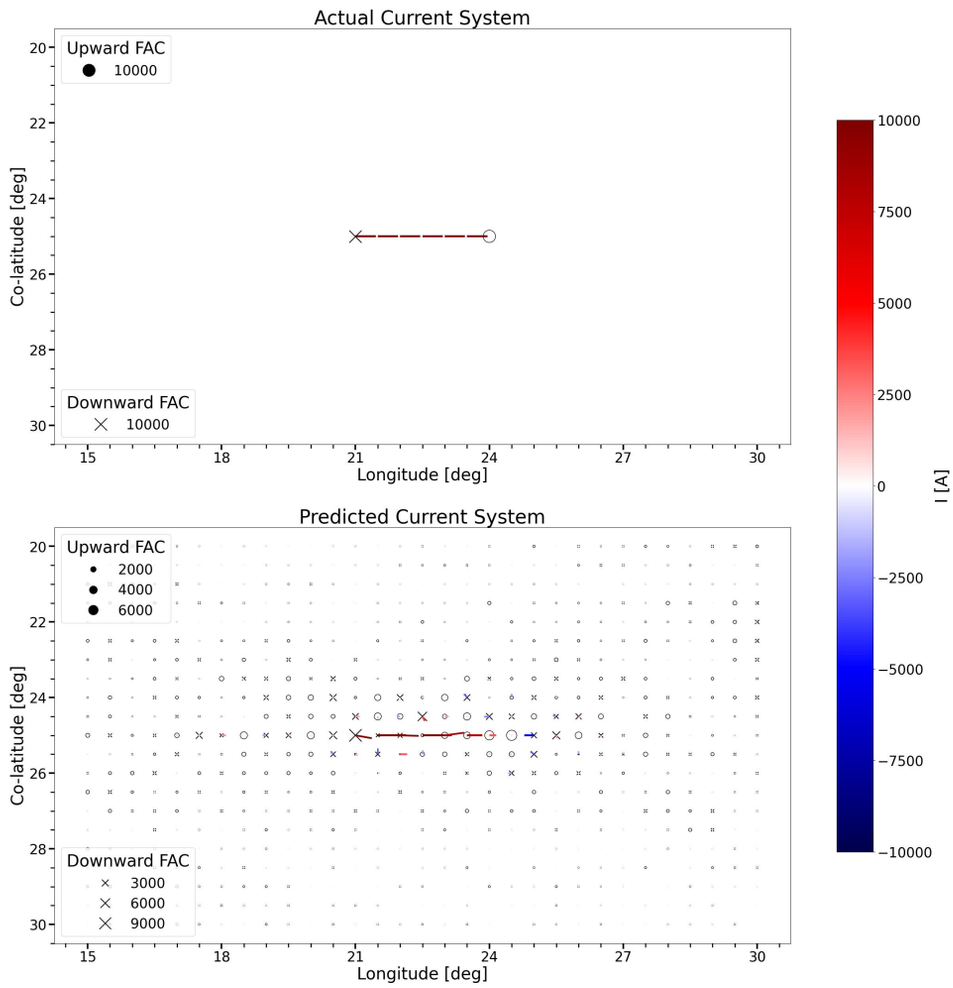

Figure 4.4: Vectorfield of the actual (top) and estimated (bottom) current system of a 10kA downward FAC coming in at (20°co-lat., 21°long.) and travelling east 3° before travelling as an upward FAC at (20°co-lat., 24°long.). The estimated system manages to estimate the actual current system reasonably well, with a small error in the upward FAC being spread out over two grid points. The estimated system also contain a fair amount of noisy FACs. The estimated system has a mean absolute error of $2.13 \cdot 10^{-2}$.

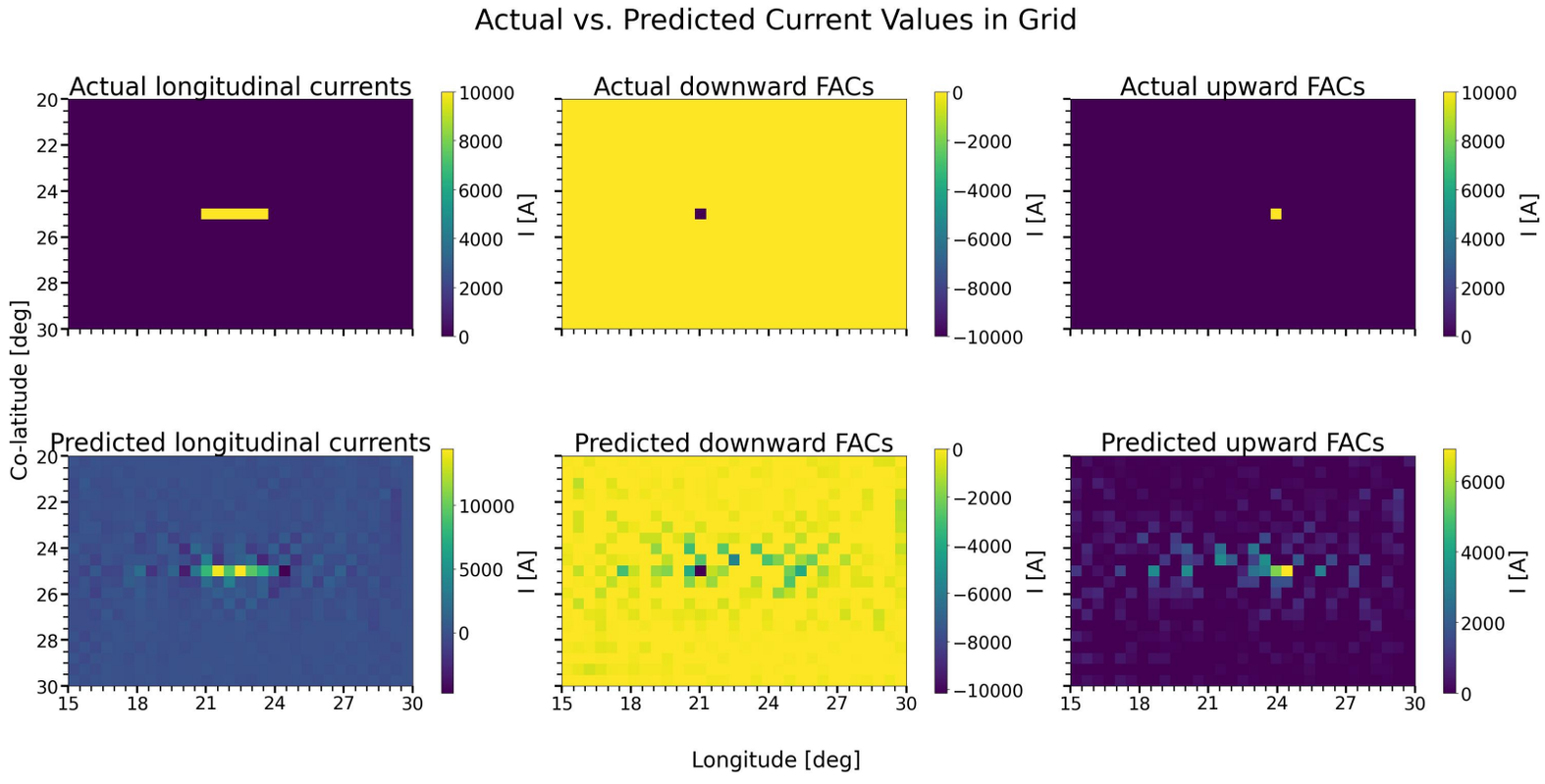

Figure 4.5: The actual (top) and estimated (bottom) longitudinal current (left), downward FAC (center) and upward FAC (right) grid values for a current system of a 10kA downward FAC coming in at (20°co-lat., 21°long.) and travelling east 3° before travelling as an upward FAC at (20°co-lat., 24°long.). The estimated system is reasonably accurate to the the actual values with some reduction in the resolution of the upward FAC which have been spread out over two grid points, while some noisy FAC values occur around the current system.

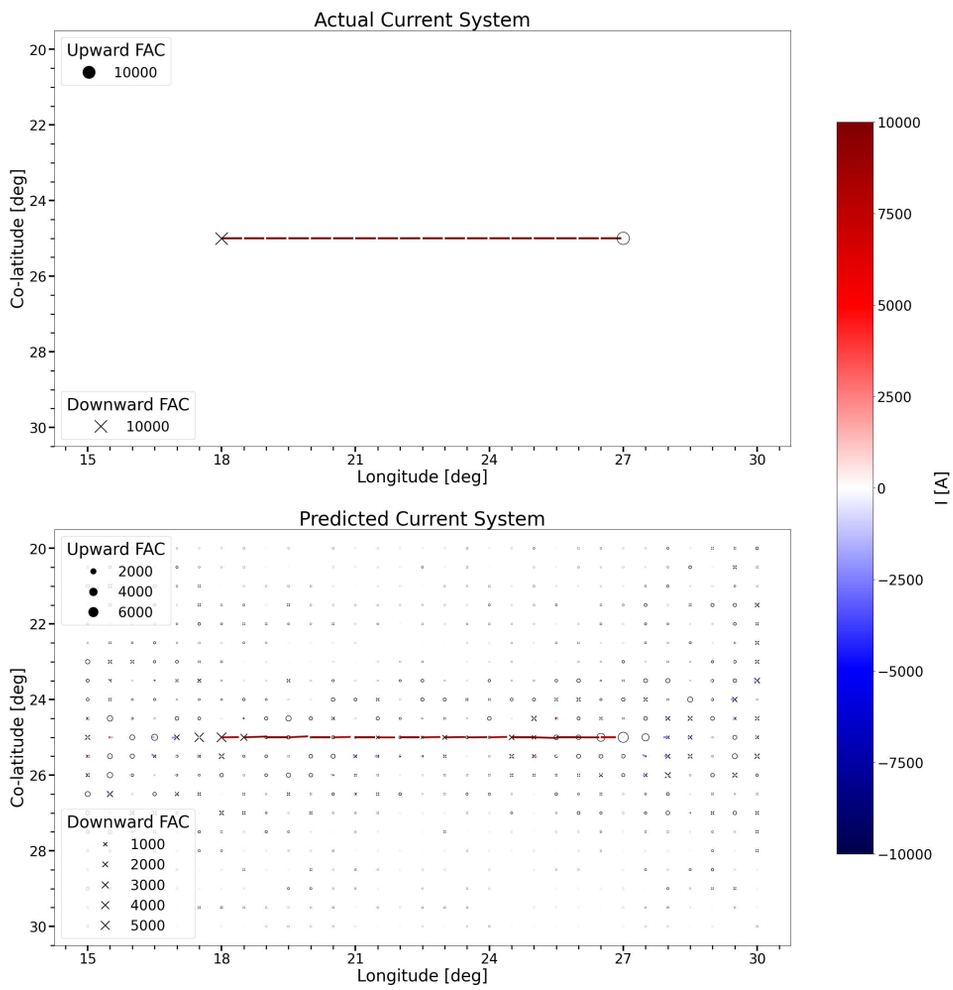

Figure 4.6: Vectorfield of the actual (top) and estimated (bottom) current system of a 10kA downward FAC coming in at (20°co-lat., 18°long.) and travelling east 9° before travelling as an upward FAC at (20°co-lat., 27°long.). The estimated system manages to estimate the actual current system reasonably well, with some error in the FACs being spread out over two or three grid points and some noisy FACs surrounding the current system. The estimated system has a mean absolute error of $2.36 \cdot 10^{-2}$.

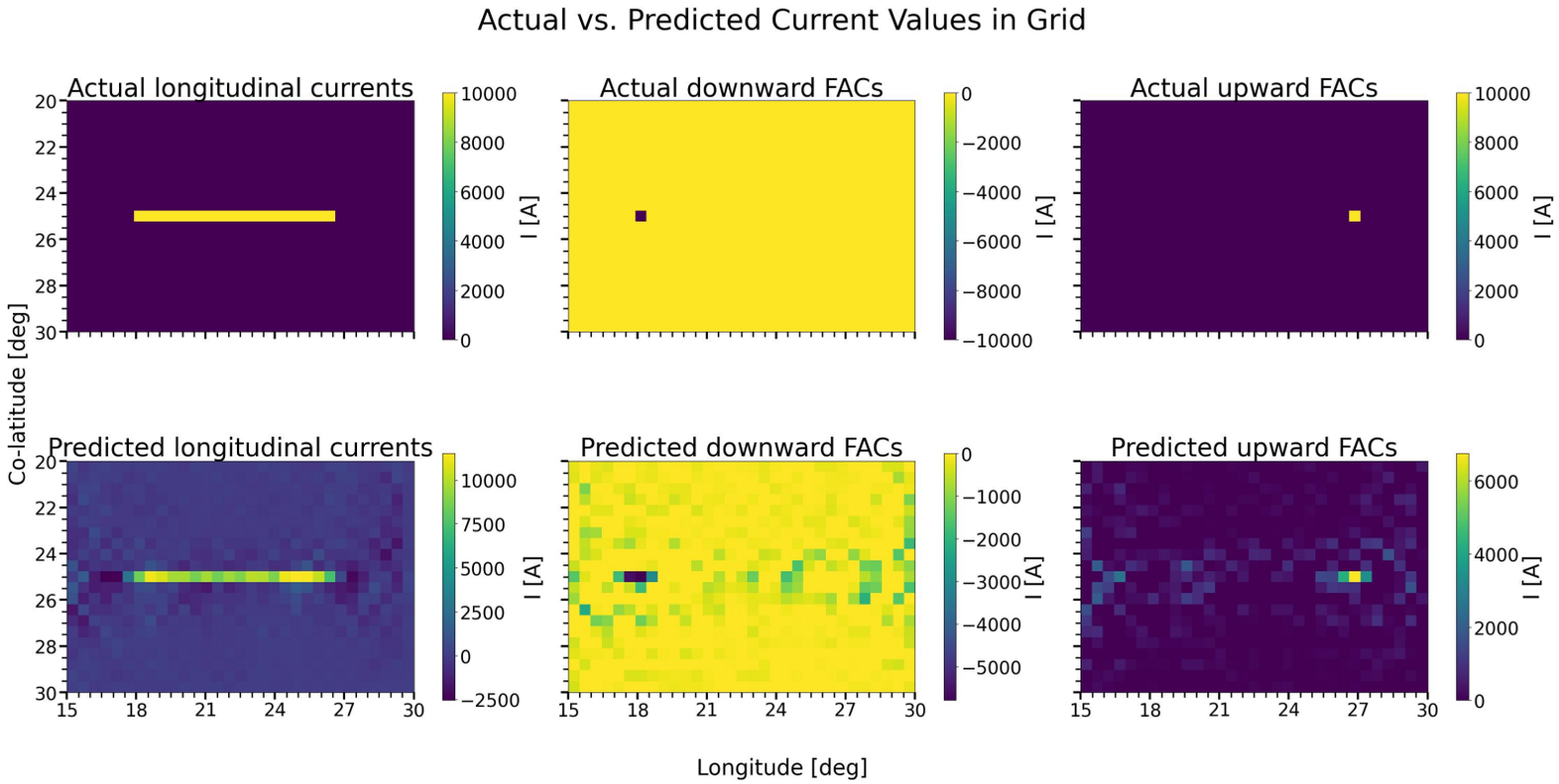

Figure 4.7: The actual (top) and estimated (bottom) longitudinal current (left), downward FAC (center) and upward FAC (right) grid values for a current system of a 10kA downward FAC coming in at (20°co-lat., 18°long.) and travelling east 9° before travelling as an upward FAC at (20°co-lat., 27°long.). The estimated system is reasonably accurate to the the actual values with some reduction in the resolution of the FACs as they spread out over two or three grid points, while some noisy FAC values occur around the current system.

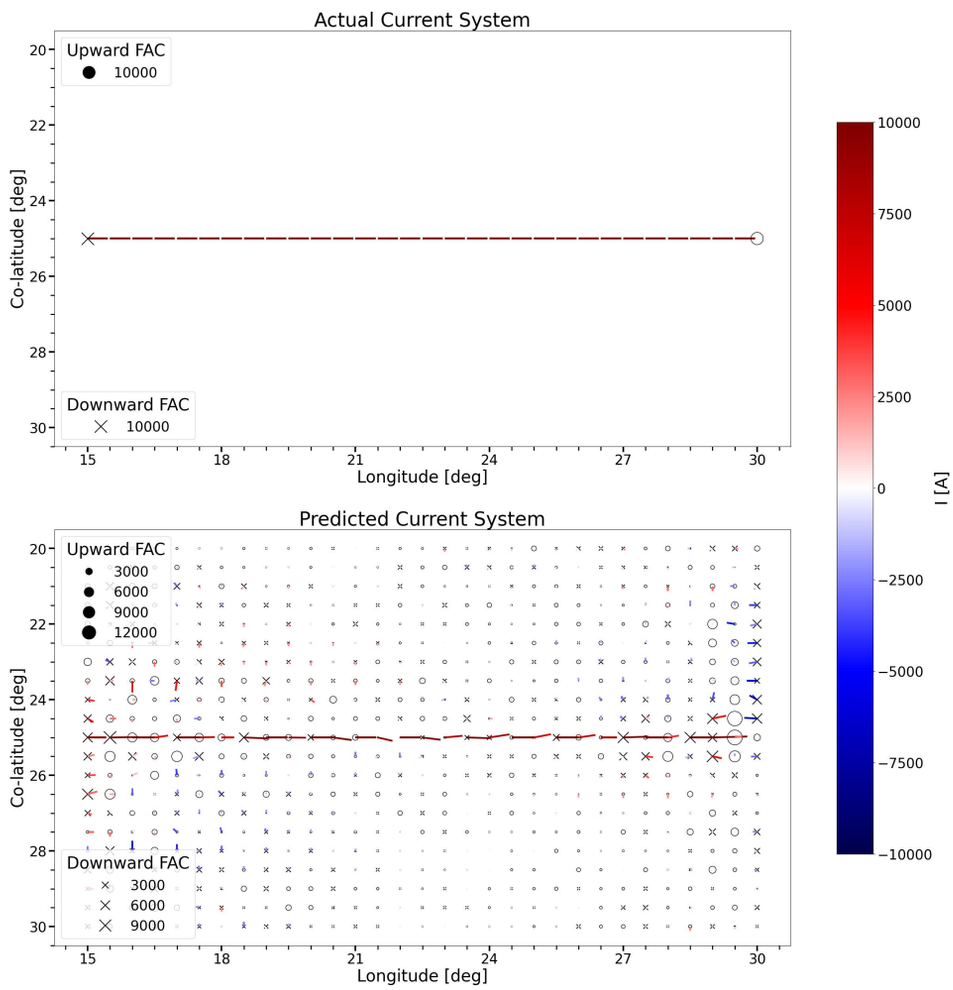

Figure 4.8: Vectorfield of the actual (top) and estimated (bottom) current system of a 10kA downward FAC coming in at (20°co-lat., 15°long.) and travelling east 15° before travelling as an upward FAC at (20°co-lat., 30°long.). The estimated system manages to estimate the actual current system reasonably well around the middle of the grid, but it becomes more error prone at the grid edges leading to poor estimation of the FACs and exhibiting noisy horizontal currents and FACs. The estimated system has a mean absolute error of $4.26 \cdot 10^{-2}$.

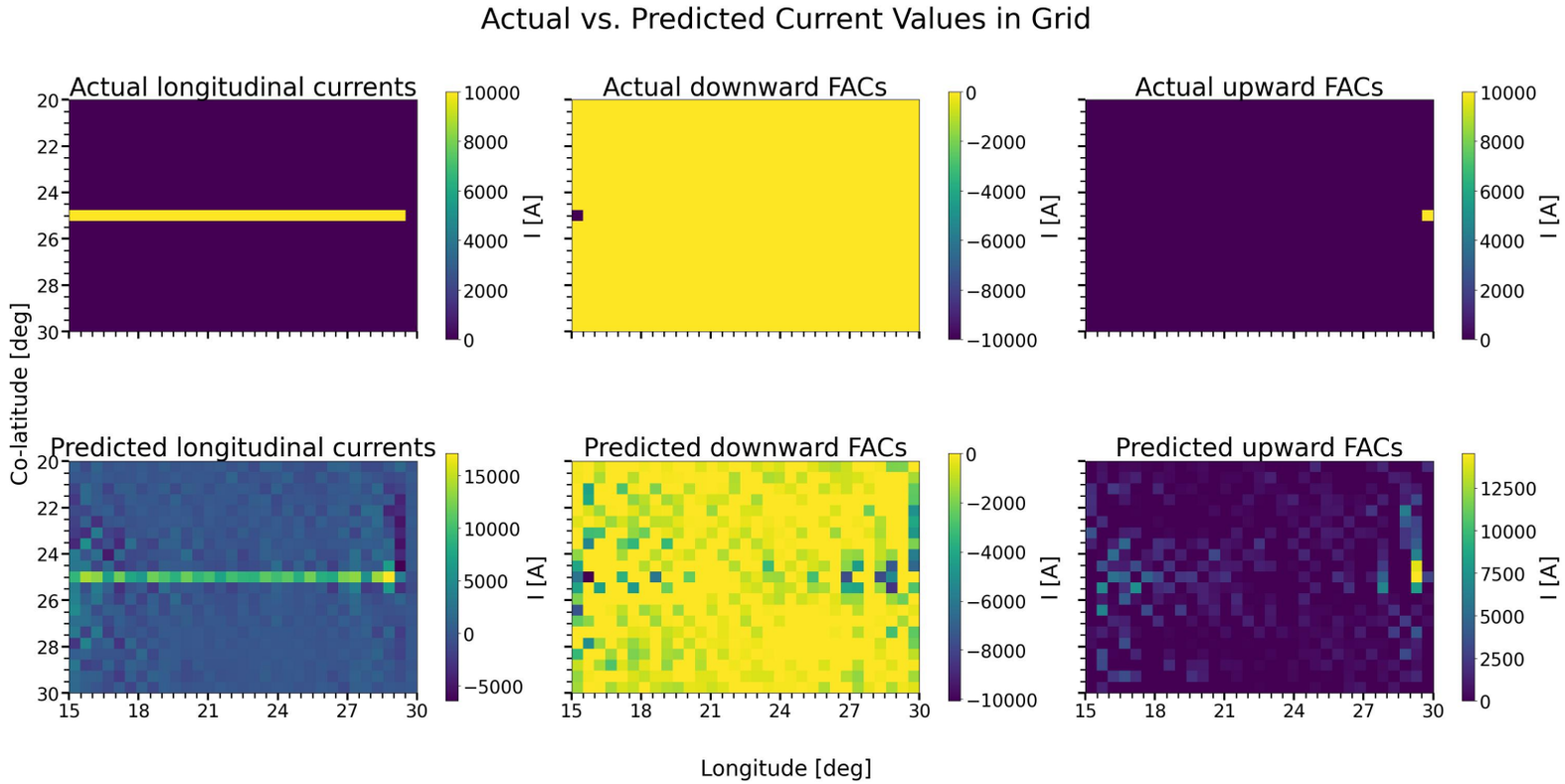

Figure 4.9: The actual (top) and estimated (bottom) longitudinal current (left), downward FAC (center) and upward FAC (right) grid values for a current system of a 10kA downward FAC coming in at (20°co-lat., 15°long.) and travelling east 15° before travelling as an upward FAC at (20°co-lat., 30°long.). The estimated system is reasonably accurate to the the actual values around the middle of the grid but it becomes more error prone at the grid edges exhibiting noisy current values in all directions.

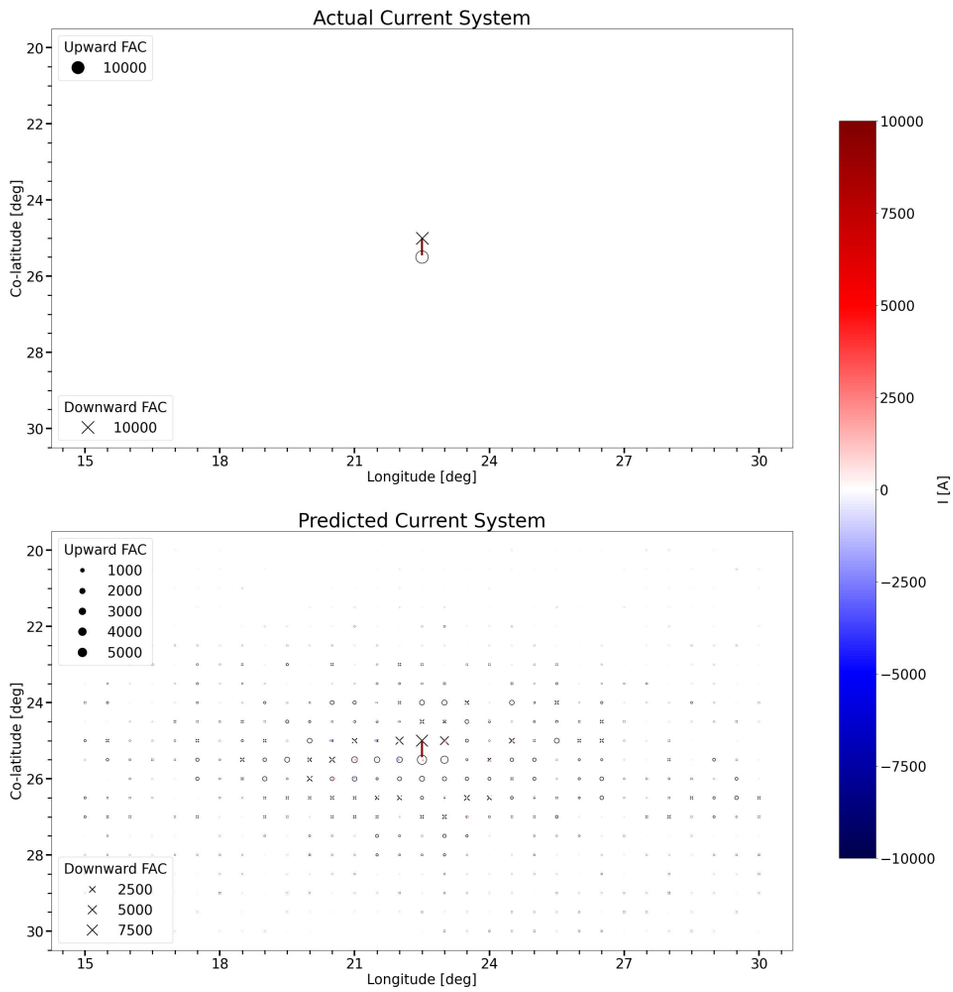

Figure 4.10: Vectorfield of the actual (top) and estimated (bottom) current system of a 10kA downward FAC coming in at (25°co-lat., 22.5°long.) and travelling south 0.5° before travelling as an upward FAC at (25.5°co-lat., 22.5°long.). The estimated system manages to estimate the actual current system reasonably well, with some error in the FACs being spread out over neighbouring grid points and some noisy FACs around the current system. The estimated system has a mean absolute error of $3.67 \cdot 10^{-2}$.

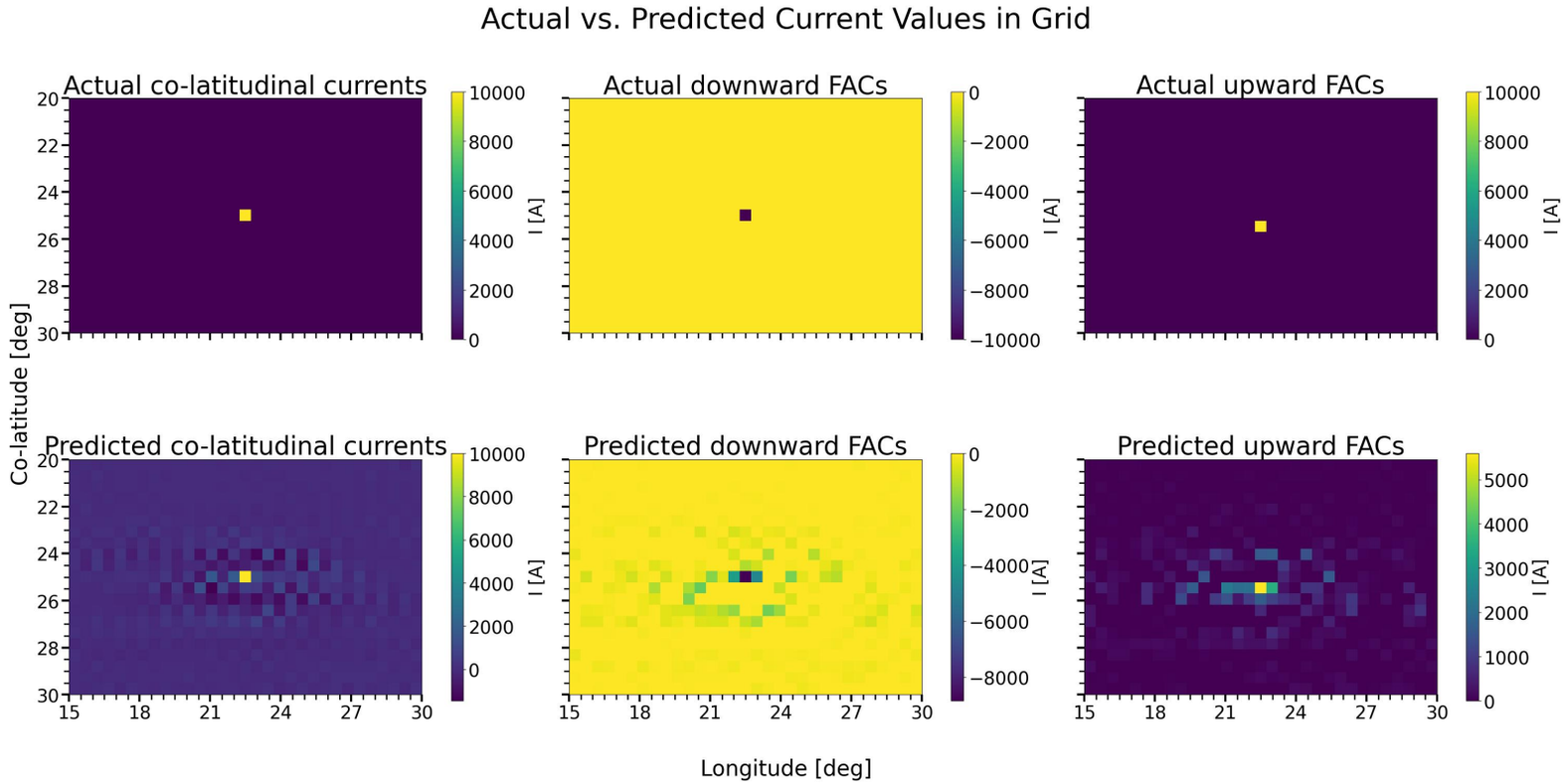

Figure 4.11: The actual (top) and estimated (bottom) co-latitudinal current (left), downward FAC (center) and upward FAC (right) grid values for a current system of a 10kA downward FAC coming in at (25°co-lat., 22.5°long.) and travelling south 0.5° before travelling as an upward FAC at (25.5°co-lat., 22.5°long.). The co-latitudinal values are reasonably well estimated, while the estimated FAC values have a reduced resolution of about three grid points along the longitudinal direction.

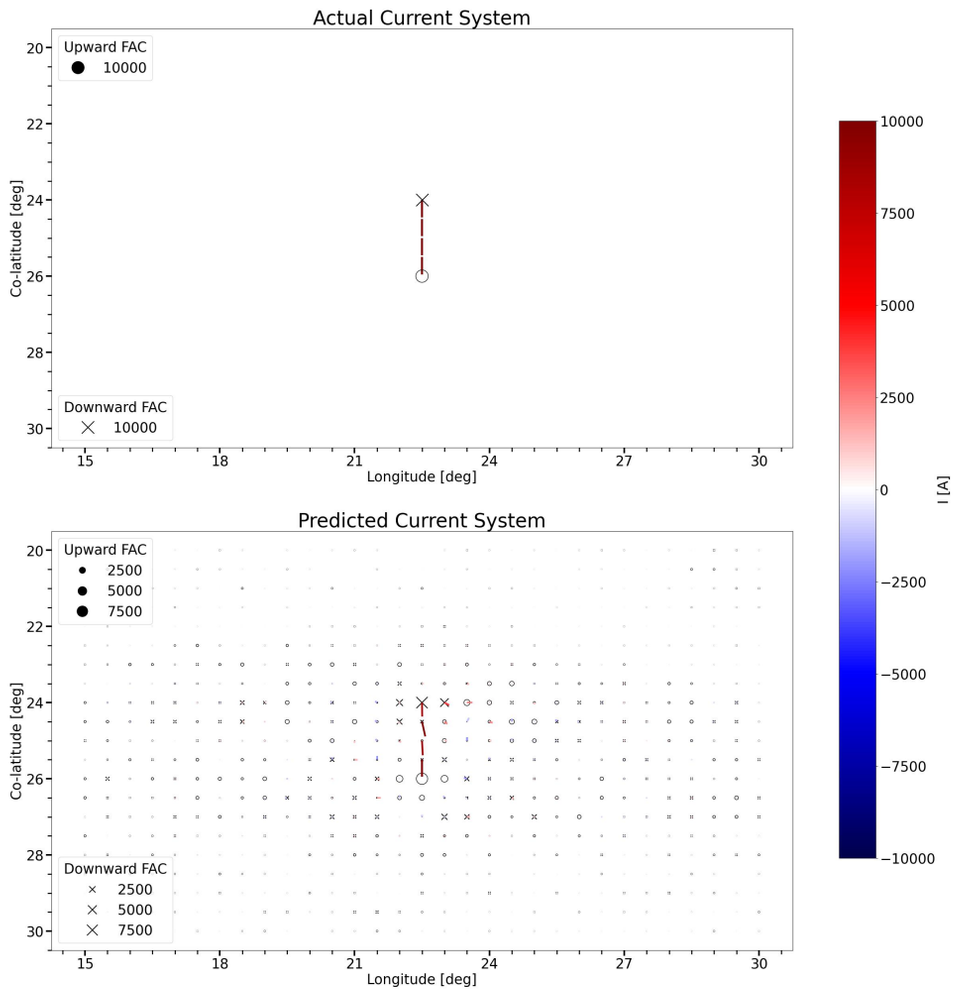

Figure 4.12: Vectorfield of the actual (top) and estimated (bottom) current system of a 10kA downward FAC coming in at (24°co-lat., 22.5°long.) and travelling south 2° before travelling as an upward FAC at (26°co-lat., 22.5°long.). The estimated system manages to estimate the actual current system reasonably well, with some error in the FACs being spread out over neighbouring grid points and some noisy FACs around the current system. The estimated system has a mean absolute error of $2.27 \cdot 10^{-2}$.

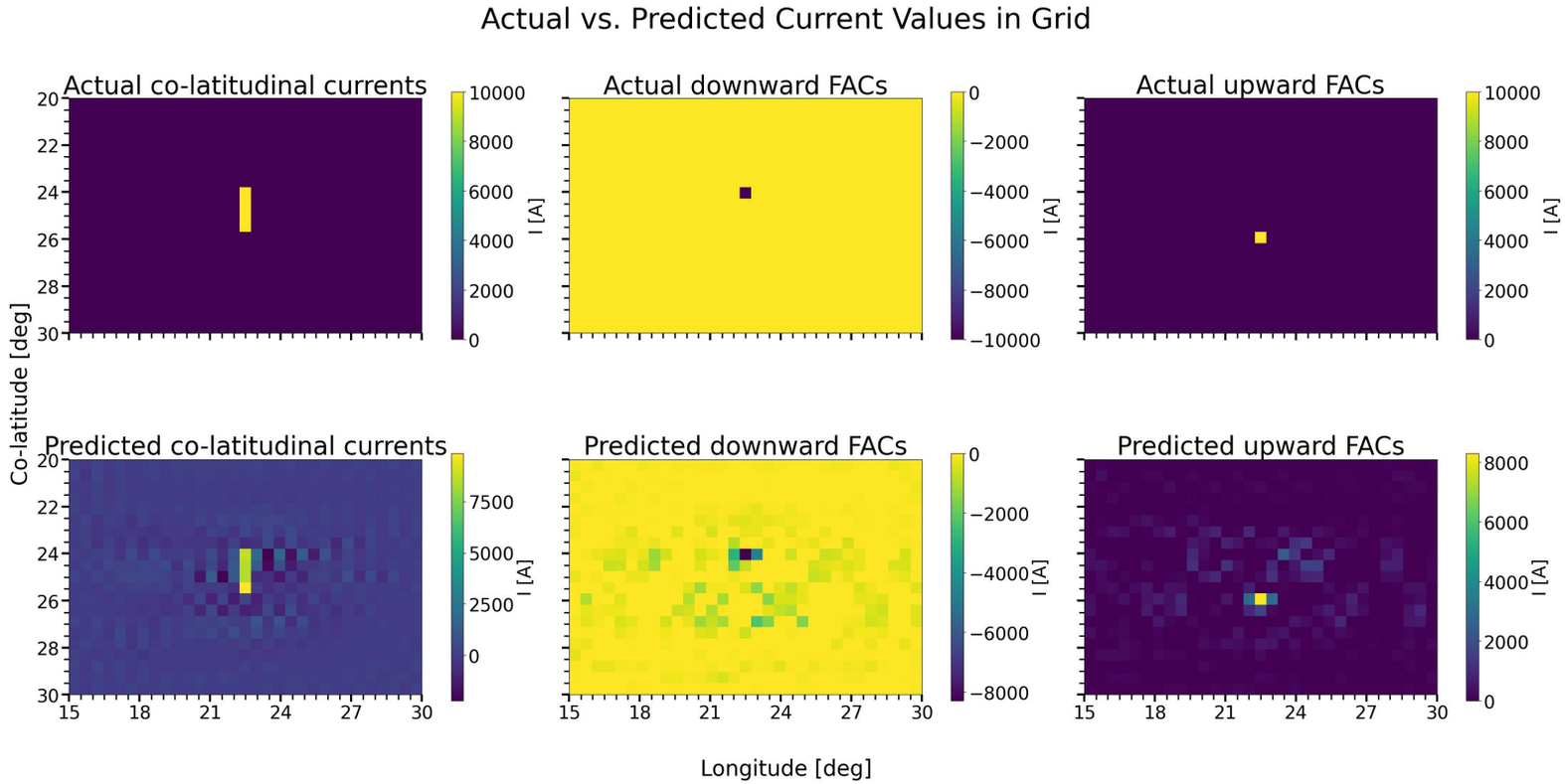

Figure 4.13: The actual (top) and estimated (bottom) co-latitudinal current (left), downward FAC (center) and upward FAC (right) grid values for a current system of a 10kA downward FAC coming in at (24°co-lat., 22.5°long.) and travelling south 2° before travelling as an upward FAC at (26°co-lat., 22.5°long.). The co-latitudinal values are reasonably well estimated, while the estimated FAC values have a reduced resolution of about three grid points along the longitudinal direction.

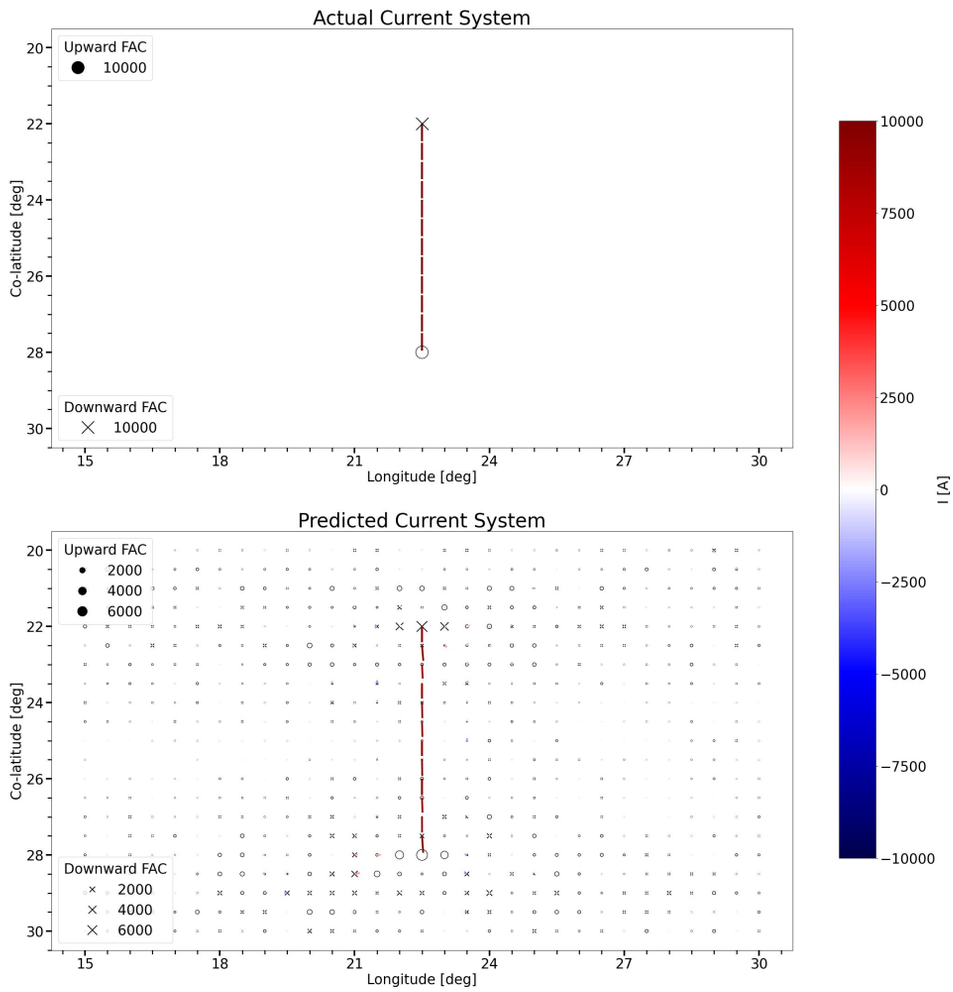

Figure 4.14: Vectorfield of the actual (top) and estimated (bottom) current system of a 10kA downward FAC coming in at (22°co-lat., 22.5°long.) and travelling south 6° before travelling as an upward FAC at (28°co-lat., 22.5°long.). The estimated system manages to estimate the actual current system reasonably well, with some error in the FACs being spread out over neighbouring grid points and some noisy FACs around the current system. The estimated system has a mean absolute error of $2.69 \cdot 10^{-2}$.

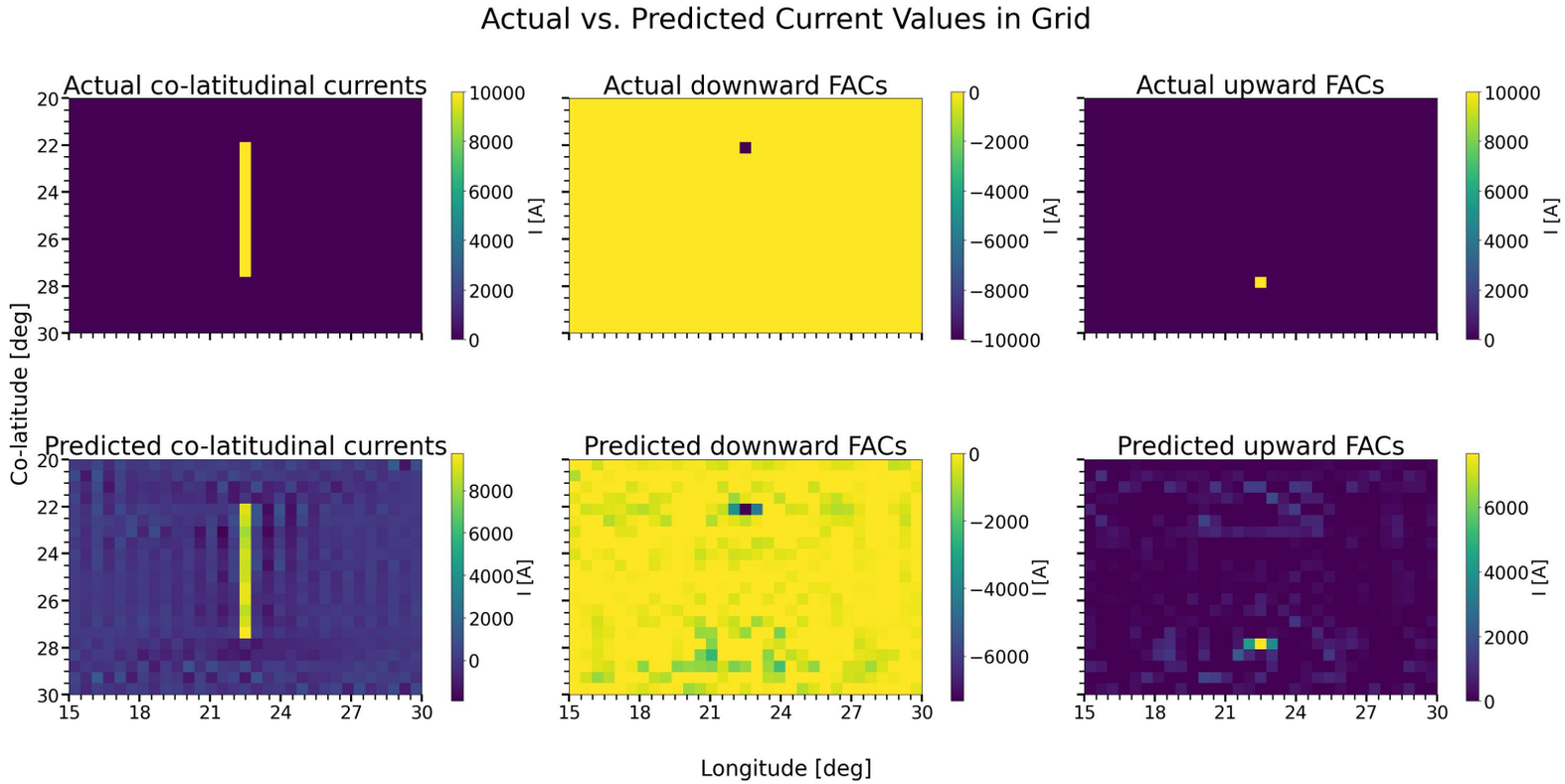

Figure 4.15: The actual (top) and estimated (bottom) co-latitudinal current (left), downward FAC (center) and upward FAC (right) grid values for a current system of a 10kA downward FAC coming in at (22°co-lat., 22.5°long.) and travelling south 6° before travelling as an upward FAC at (28°co-lat., 22.5°long.). The co-latitudinal values are reasonably well estimated, while the estimated FAC values have a reduced resolution of about three grid points along the longitudinal direction.

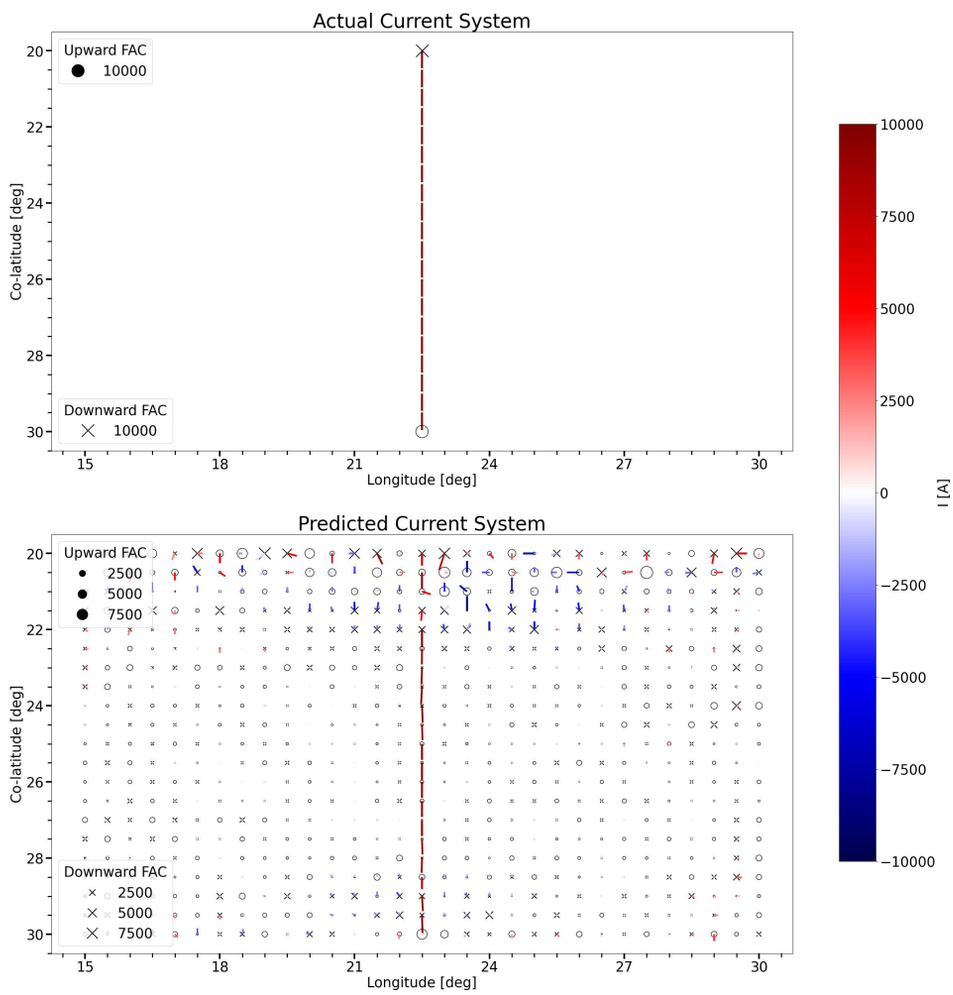

Figure 4.16: Vectorfield of the actual (top) and estimated (bottom) current system of a 10kA downward FAC coming in at (20°co-lat., 22.5°long.) and travelling south 10° before travelling as an upward FAC at (30°co-lat., 22.5°long.). The estimated system manages to estimate the actual current system reasonably well around the middle of the grid, but it becomes more error prone at the grid edges leading to poor estimation of the FACs and exhibiting noisy horizontal currents and FACs. The estimated system has a mean absolute error of $3.45 \cdot 10^{-2}$.

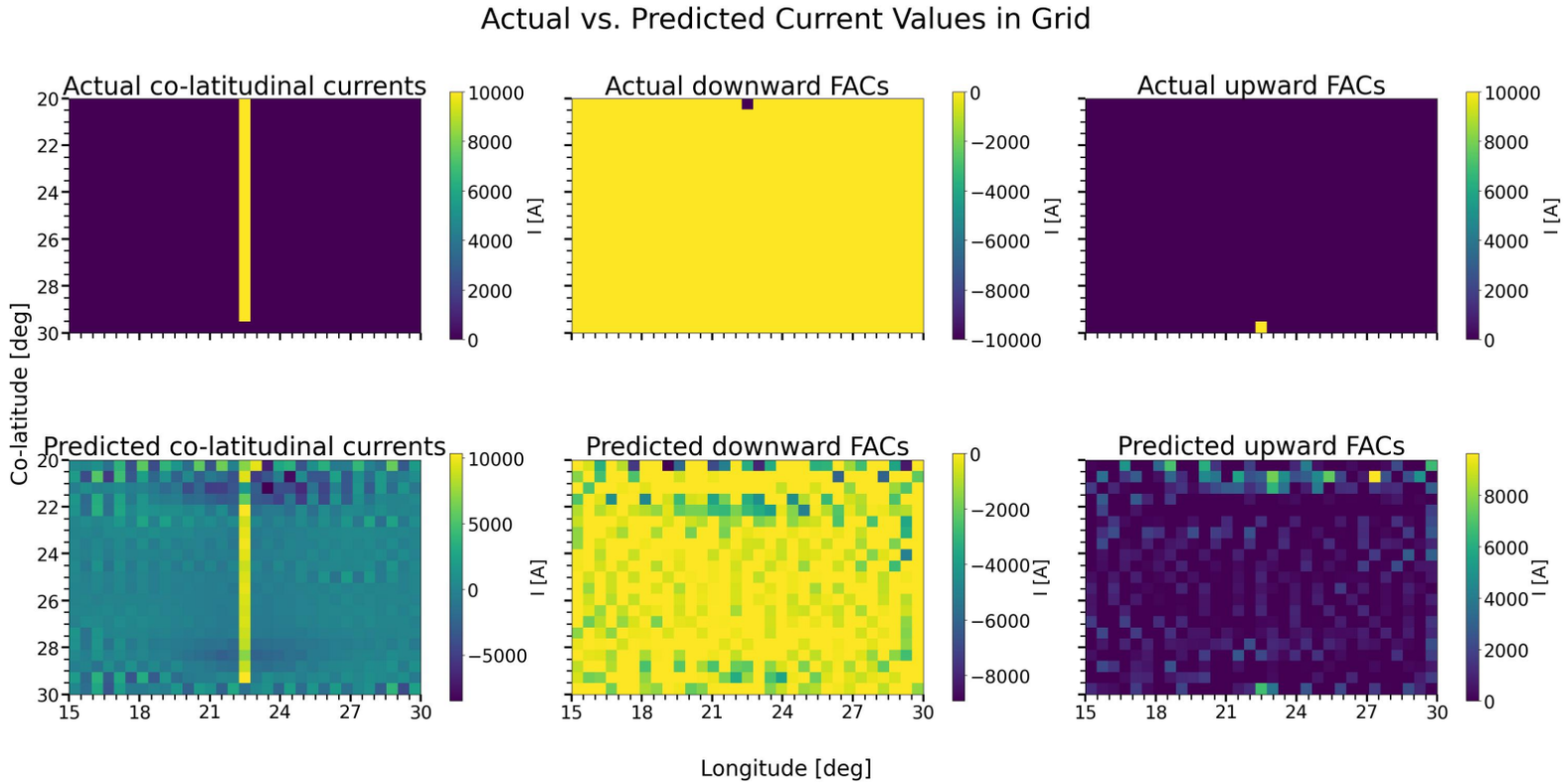

Figure 4.17: The actual (top) and estimated (bottom) co-latitudinal current (left), downward FAC (center) and upward FAC (right) grid values for a current system of a 10kA downward FAC coming in at (22°co-lat., 22.5°long.) and travelling south 6° before travelling as an upward FAC at (28°co-lat., 22.5°long.). The estimated system is reasonably accurate to the the actual values around the middle of the grid but it becomes more error prone at the grid edges exhibiting noisy current values in all directions.

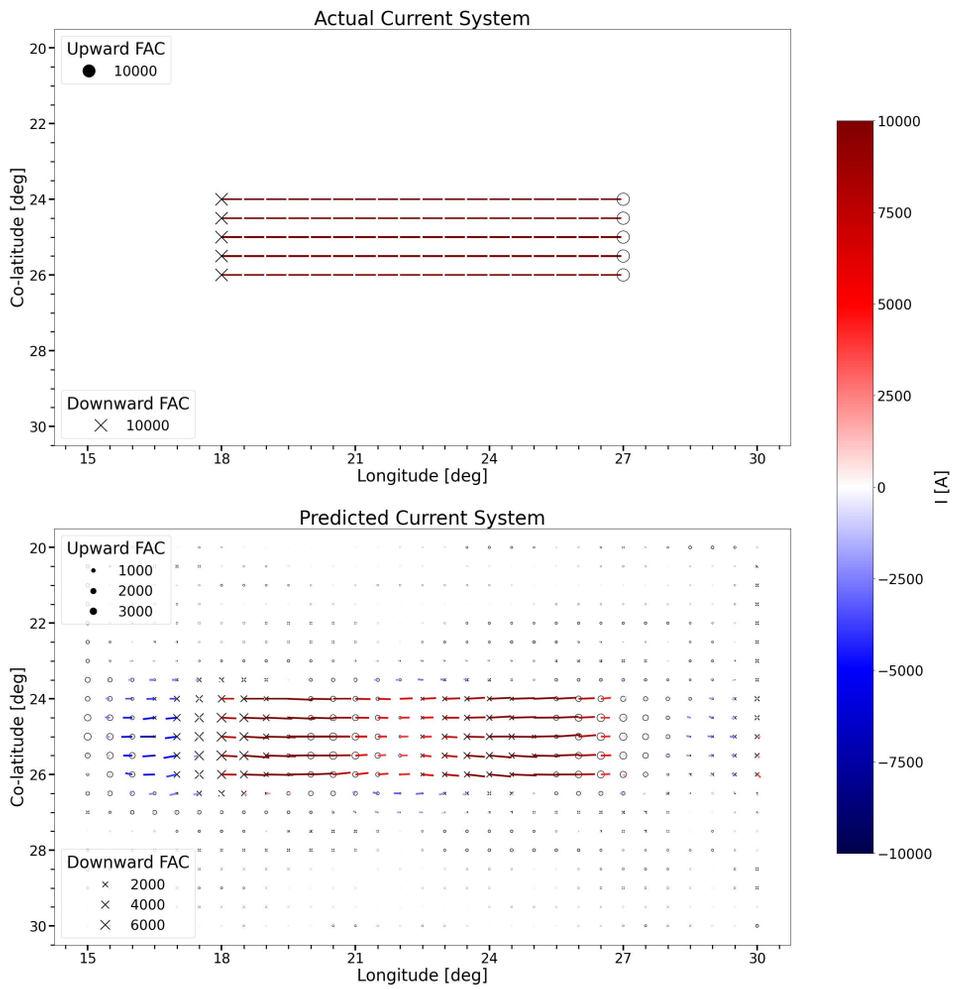

Figure 4.18: Vectorfield of the actual (top) and estimated (bottom) current system of a set of 10kA downward FACs coming in at (24° − 26°co-lat., 18°long.) and travelling east 9° before travelling as upward FACs at (24° − 26°co-lat., 27°long.). The estimated system gets the overall structure of the actual current system correct, but deviates in the middle and at the longitudinal edges of the current system. In the middle of the estimated system the eastbound currents lose power to FACs, and weak westbound currents occur at the north and south of the system edges. At the longitudinal edges of the estimated system the FACs gets spread out in the longitudinal direction, and westbound currents occur at the western edge. The estimated system has a mean absolute error of $4.91 \cdot 10^{-2}$.

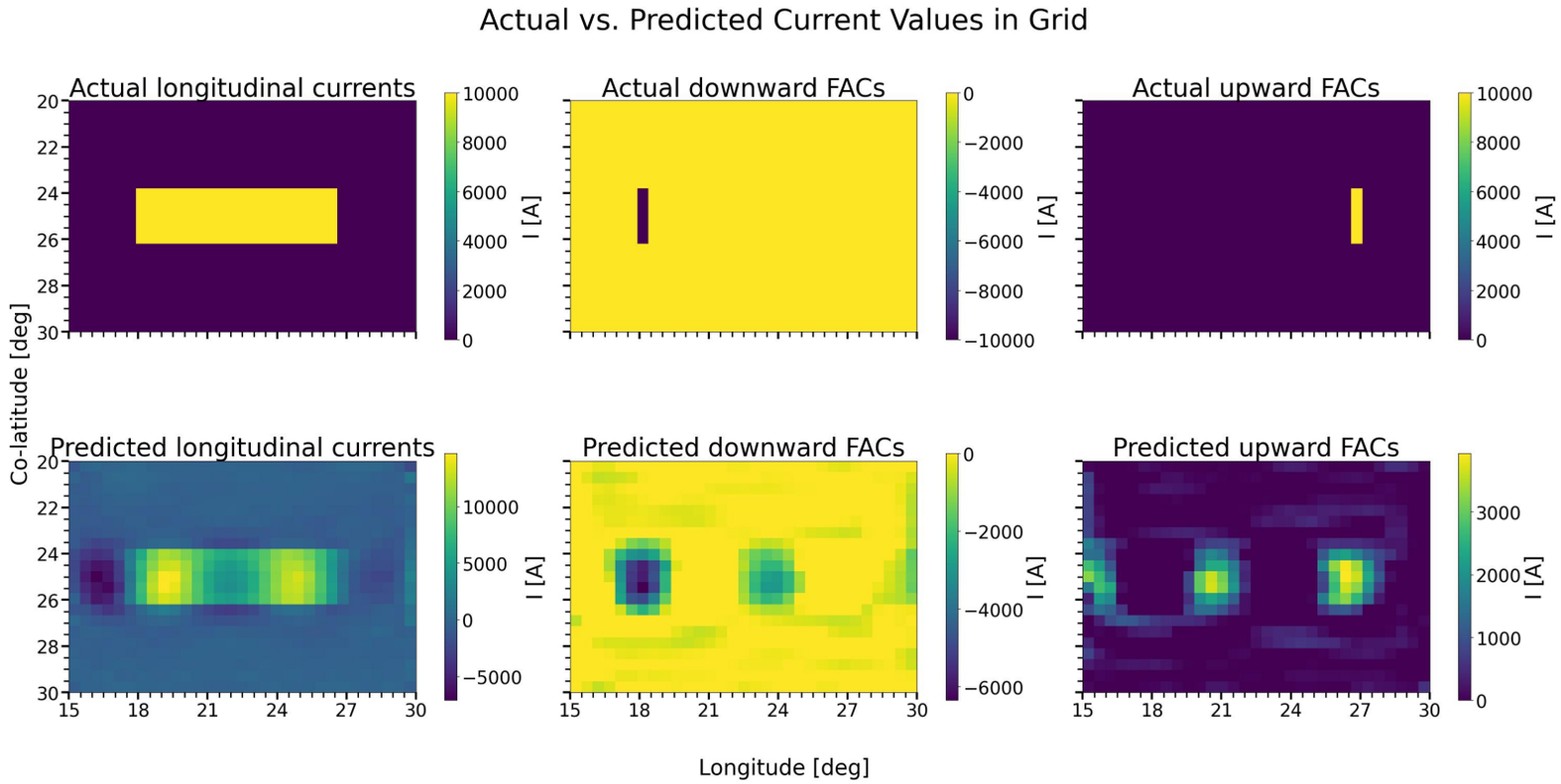

Figure 4.19: The actual (top) and estimated (bottom) longitudinal current (left), downward FAC (center) and upward FAC (right) grid values for a current system of a set of 10kA downward FACs coming in at (24° – 26°co-lat., 18°long.) and travelling east 9° before travelling as upward FACs at (24° – 26°co-lat., 27°long.). The estimated longitudinal values is overestimated at the longitudinal edges of the current system, and underestimated in the middle of and to the west of the system. The estimated FACs have a reduced resolution in both co-latitudinal and longitudinal directions and repeating artifacts occur in the longitudinal direction.

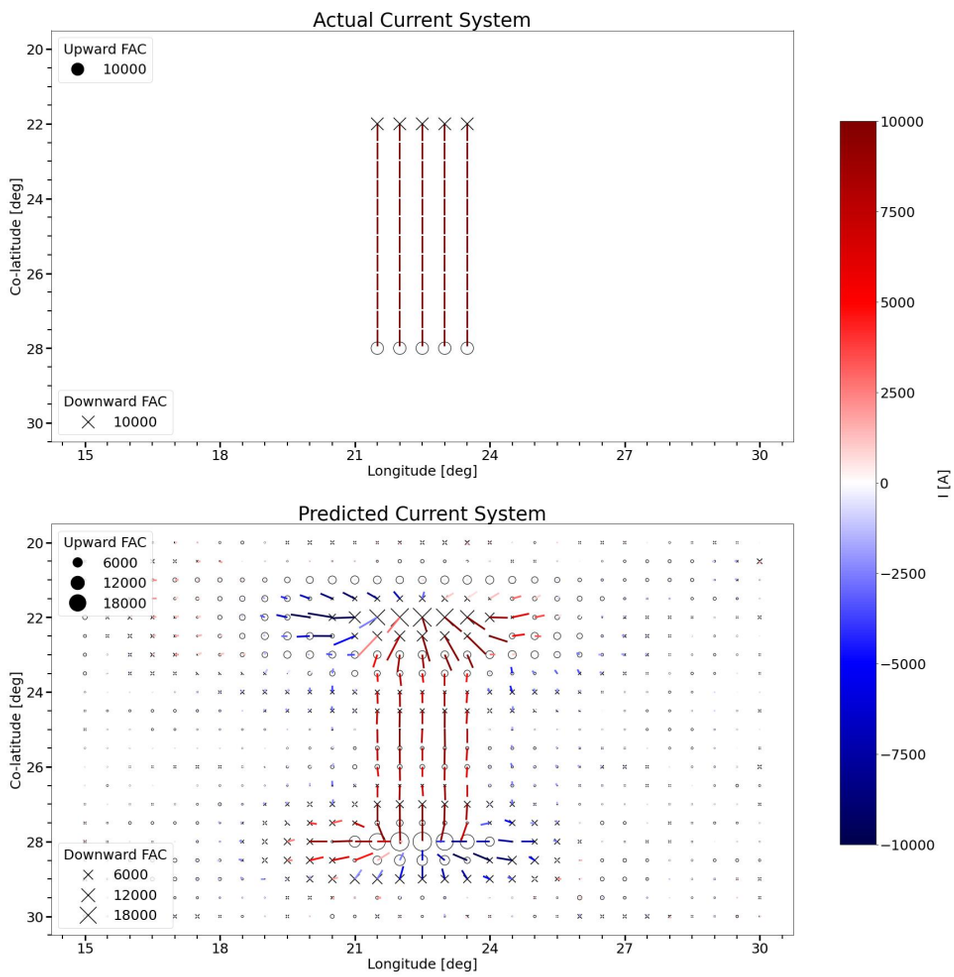

Figure 4.20: Vectorfield of the actual (top) and estimated (bottom) current system of a set of 10kA downward FACs coming in at (22°co-lat., 21.5° – 23.5°long.) and travelling south 6° before travelling as upward FACs at (28°co-lat., 21.5° – 23.5°long.). The estimated system gets the middle structure of the actual current system correct, but deviates significantly at the co-latitudinal edges of the current system. The FACs at the edges are almost doubled in amplitude with large converging horizontal currents surrounding the south edge and large diverging currents surrounding the north edge of the system. The estimated system has a mean absolute error of $3.21 \cdot 10^{-2}$.

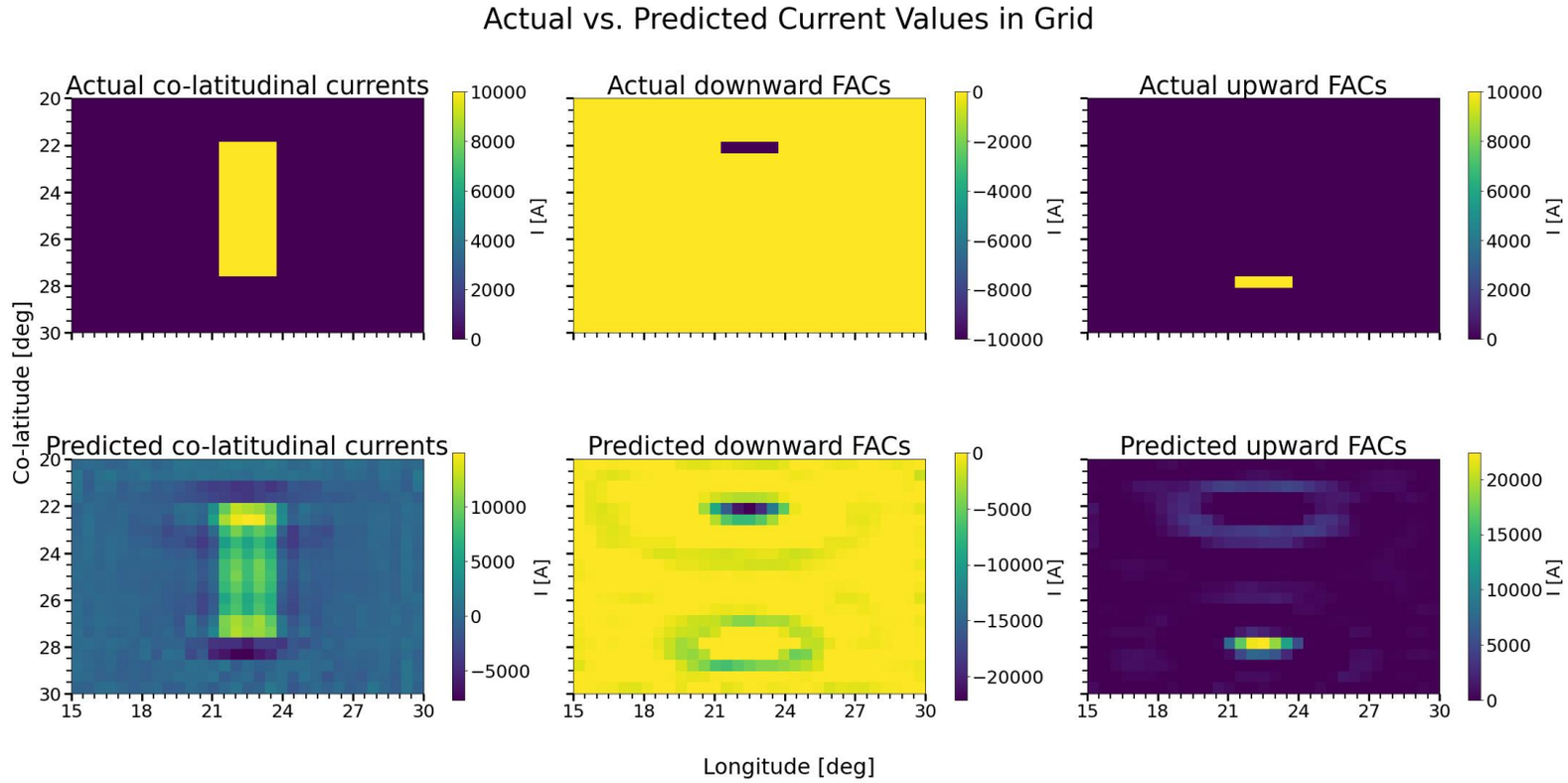

Figure 4.21: The actual (top) and estimated (bottom) longitudinal current (left), downward FAC (center) and upward FAC (right) grid values for a current system of a set of 10kA downward FACs coming in at (22°co-lat., 21.5° – 23.5°long.) and travelling south 6° before travelling as upward FACs at (28°co-lat., 21.5° – 23.5°long.). The estimated co-latitudinal values coincide with the actual values in the middle of the current system, but are overestimated around the north edge and underestimated around the south edge of the current system. The estimated FAC values have a relatively accurate resolution but are significantly overestimated in magnitude with a ring of opposite FAC values surrounding them.

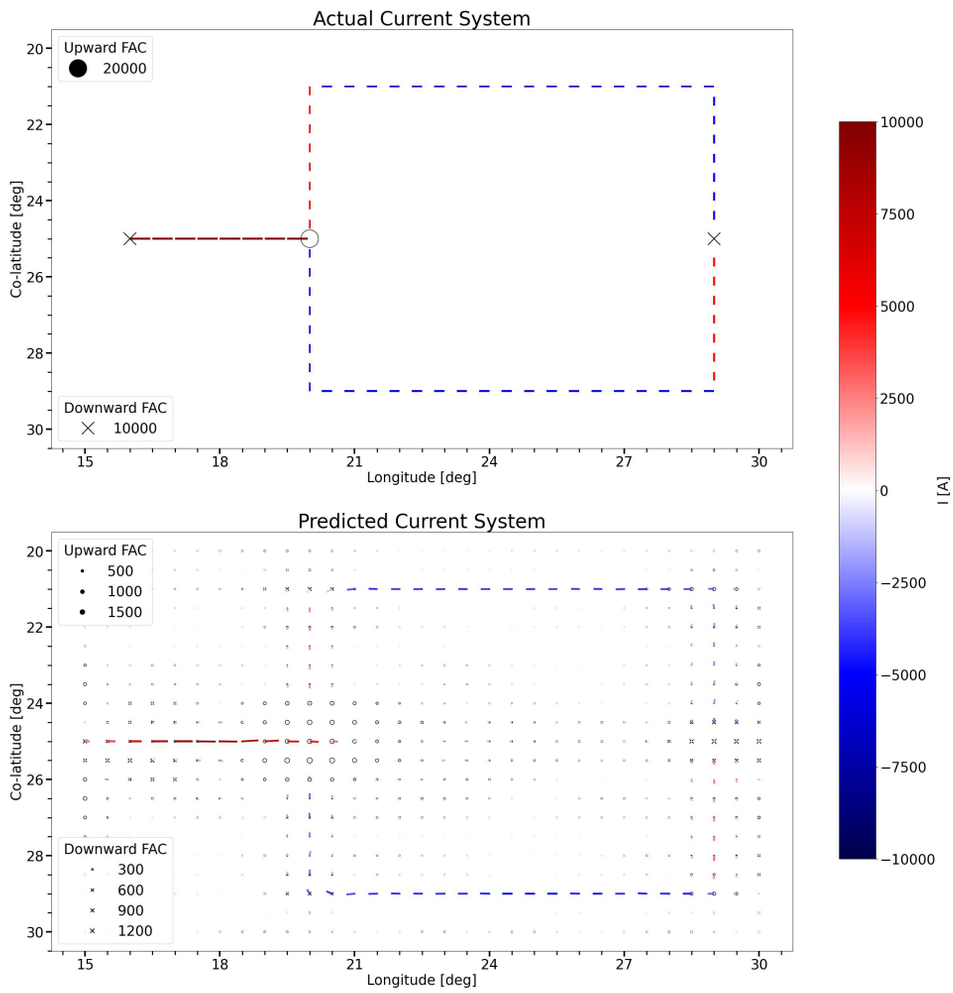

Figure 4.22: Vectorfield of the actual (top) and estimated (bottom) current system of a set of northward, southward, westward and eastward currents and upward and downward FACs. At (25°co-lat., 29°long.) a 10kA downward FAC comes in and diverges north and south at 5000A each, both travelling 4° and then travelling 9° west before moving towards eachother by 4° again and converging at (25°co-lat., 20°long.). A second 10kA downward FAC comes in at (25°co-lat., 16°long.) and travels east 4° merging with the other currents at (25°co-lat., 20°long.) and travelling as an 20000A upward FAC. The estimated system has relatively accurate longitudinal currents compared to the actual current system, but poor accuracy for the co-latitudinal currents and FACs. The estimated system has a mean absolute error of $2.52 \cdot 10^{-2}$.

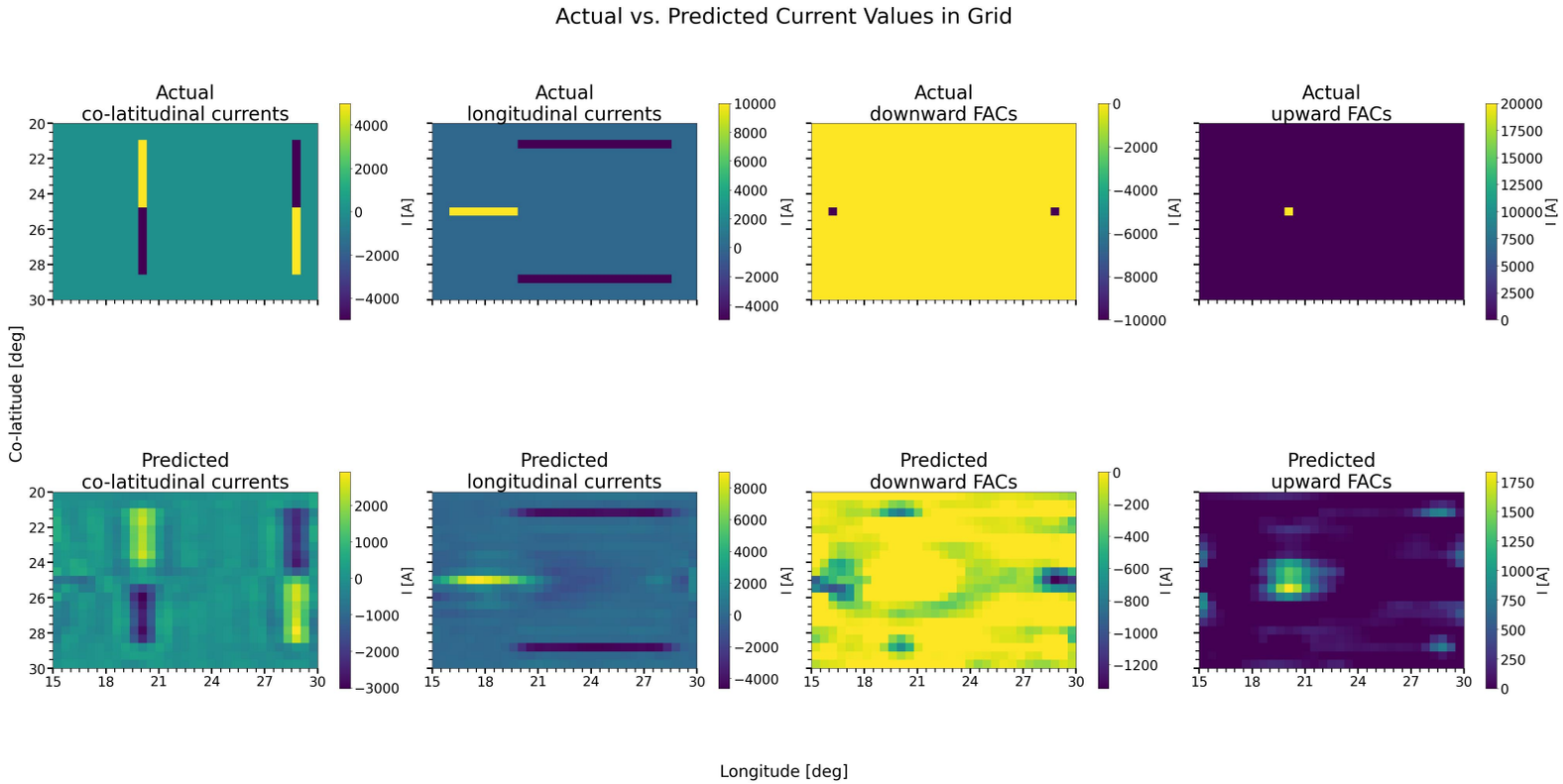

Figure 4.23: The actual (top) and estimated (bottom) co-latitudinal current (left), longitudinal current (center left), downward FAC (center right) and upward FAC (right) grid values for a current system of a set of northward, southward, westward and eastward currents and upward and downward FACs. At (25°co-lat., 29°long.) a 10kA downward FAC comes in and diverges north and south at 5000A each, both travelling 4° and then travelling 9° west before moving towards eachother by 4° again and converging at (25°co-lat., 20°long.). A second 10kA downward FAC comes in at (25°co-lat., 16°long.) and travels east 4° merging with the other currents at (25°co-lat., 20°long.) and travelling as an 20000A upward FAC. The estimated horizontal values have a reduced resolution in the longitudinal direction, and the estimated co-latitudinal values are also reduced in magnitude. The estimated FACs have a reduced resolution in both co-latitudinal and longitudinal directions while also being significantly reduced in magnitude compared to the actual values.

4.2 Results for 200 magnetometer stations

In this section visuals will only be shown for the southward current stream and the multidirectional system of currents to not overwhelm the reader with too many figures.

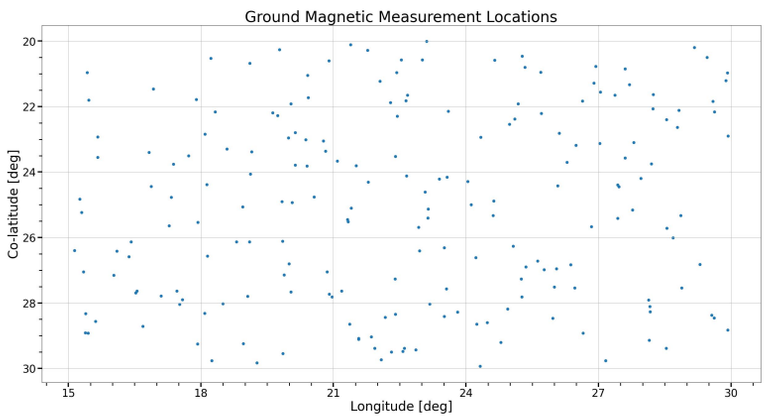

Figure 4.24: 200 randomly distributed ground magnetometer locations within 20° and 30° co-latitude and 15° and 30° longitude.

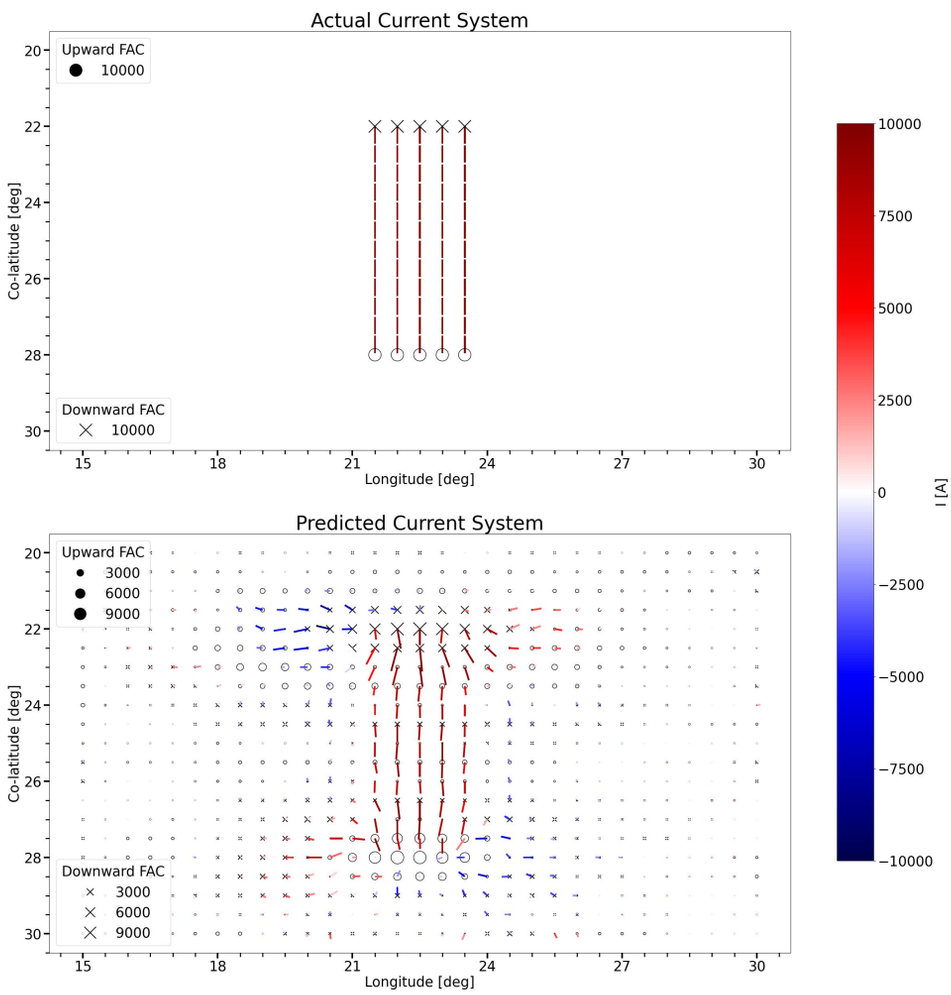

Figure 4.25: Vectorfield of the actual (top) and estimated (bottom) current system of a set of 10kA downward FACs coming in at (22°co-lat., 21.5° – 23.5°long.) and travelling south 6° before travelling as upward FACs at (28°co-lat., 21.5° – 23.5°long.). The estimated horizontal current system are relatively accurate in the middle of the current system compared to the actual currents, but becomes less accurate at the co-latitudinal edges of the current system with converging currents surrounding the south edge and diverging currents surrounding the north edge of the system. The estimated FACs at the edges are accurate to the actual FACs with some spread in the co-latitudinal direction. The estimated system has a mean absolute error of $3.94 \cdot 10^{-2}$.

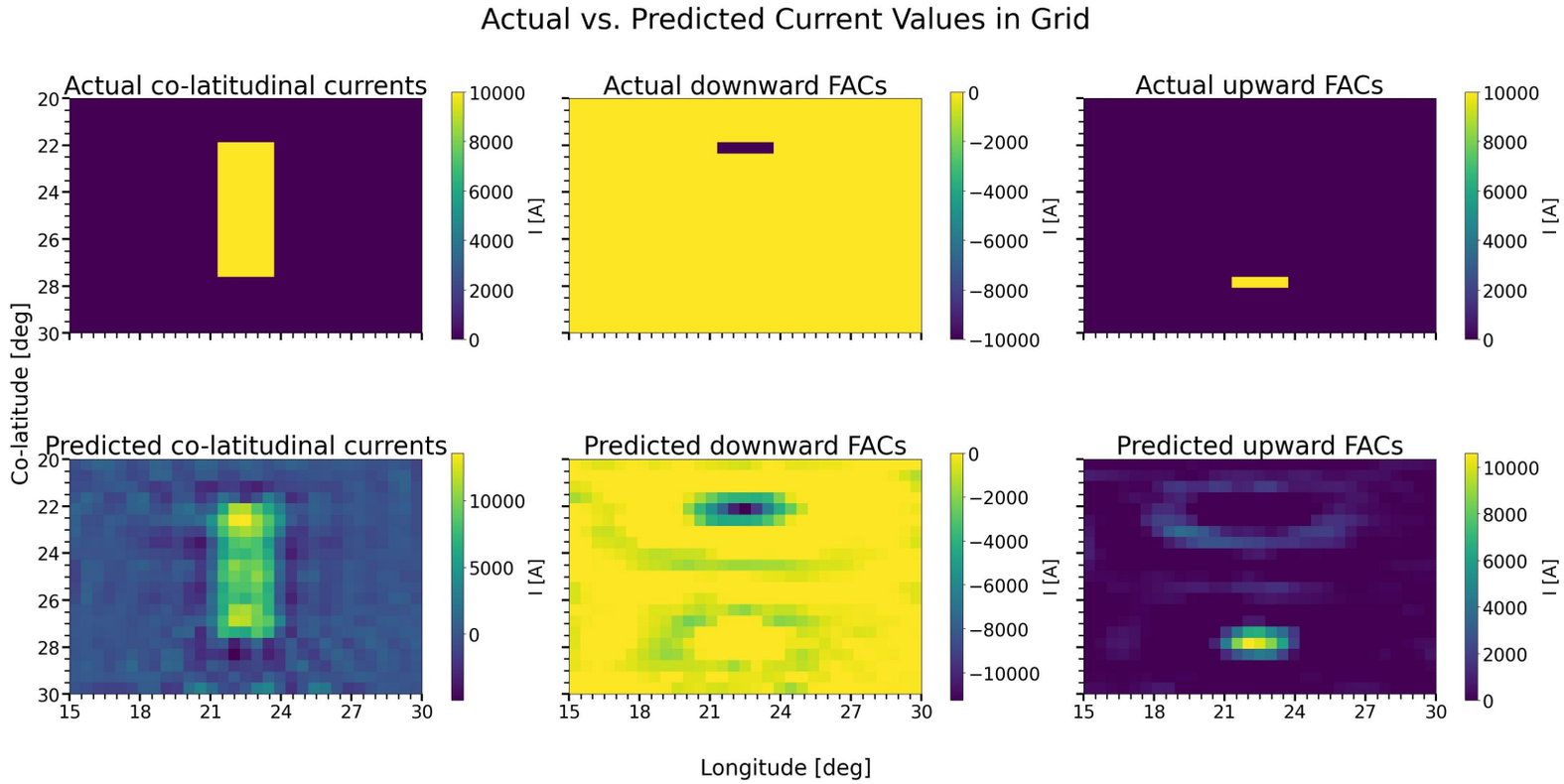

Figure 4.26: The actual (top) and estimated (bottom) longitudinal current (left), downward FAC (center) and upward FAC (right) grid values for a current system of a set of 10kA downward FACs coming in at (22°co-lat., 21.5° – 23.5°long.) and travelling south 6° before travelling as upward FACs at (28°co-lat., 21.5° – 23.5°long.). The estimated co-latitudinal values coincide with the actual values in the middle of the current system, but are overestimated around the north edge and underestimated around the south edge of the current system. The estimated FAC values are relatively accurate to the actual values, but with some loss in resolution and some noisy rings of opposite low magnitude FAC values surrounding them.

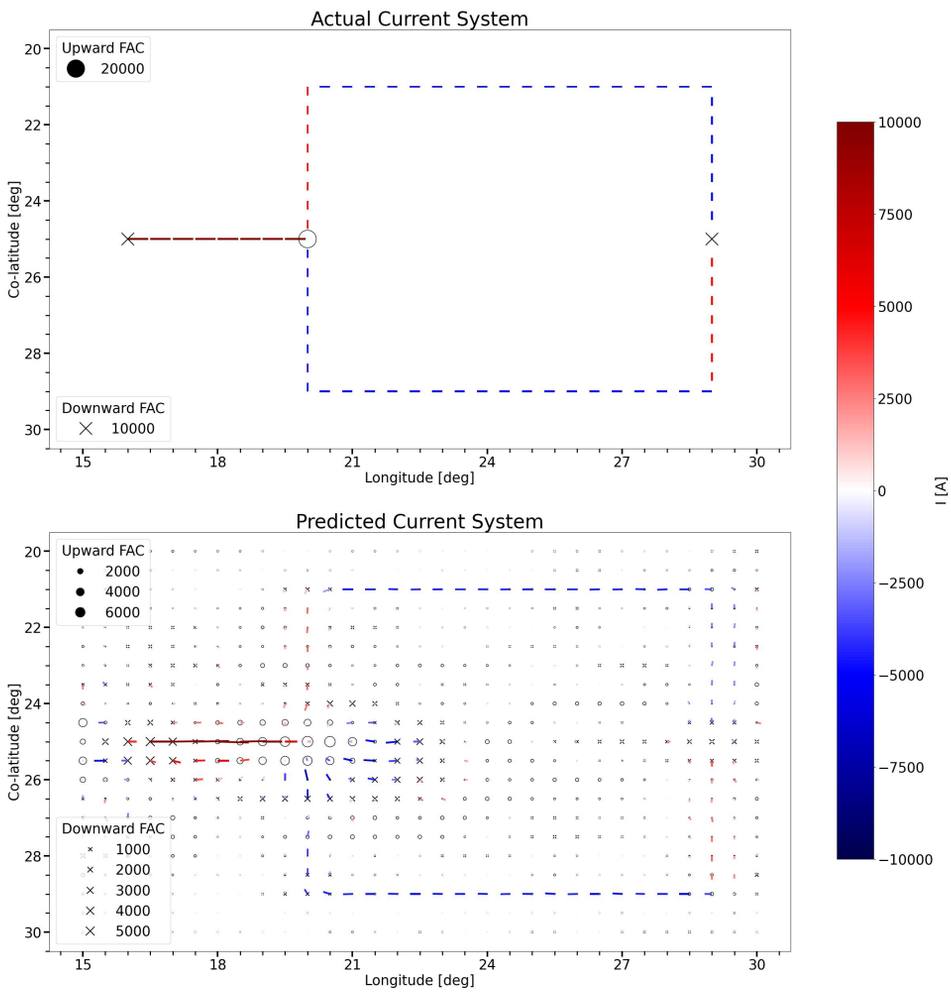

Figure 4.27: Vectorfield of the actual (top) and estimated (bottom) current system of a set of northward, southward, westward and eastward currents and upward and downward FACs. At (25°co-lat., 29°long.) a 10kA downward FAC comes in and diverges north and south at 5000A each, both travelling 4° and then travelling 9° west before moving towards eachother by 4° again and converging at (25°co-lat., 20°long.). A second 10kA downward FAC comes in at (25°co-lat., 16°long.) and travels east 4° merging with the other currents at (25°co-lat., 20°long.) and travelling as an 20000A upward FAC. The estimated system has relatively accurate longitudinal currents compared to the actual current system, but poor accuracy for the co-latitudinal currents. The estimated FACs vary in accuracy with the westernmost downward FAC and the upward FAC more accurately estimated than the easternmost downward FAC. The estimated system has a mean absolute error of $2.35 \cdot 10^{-2}$.

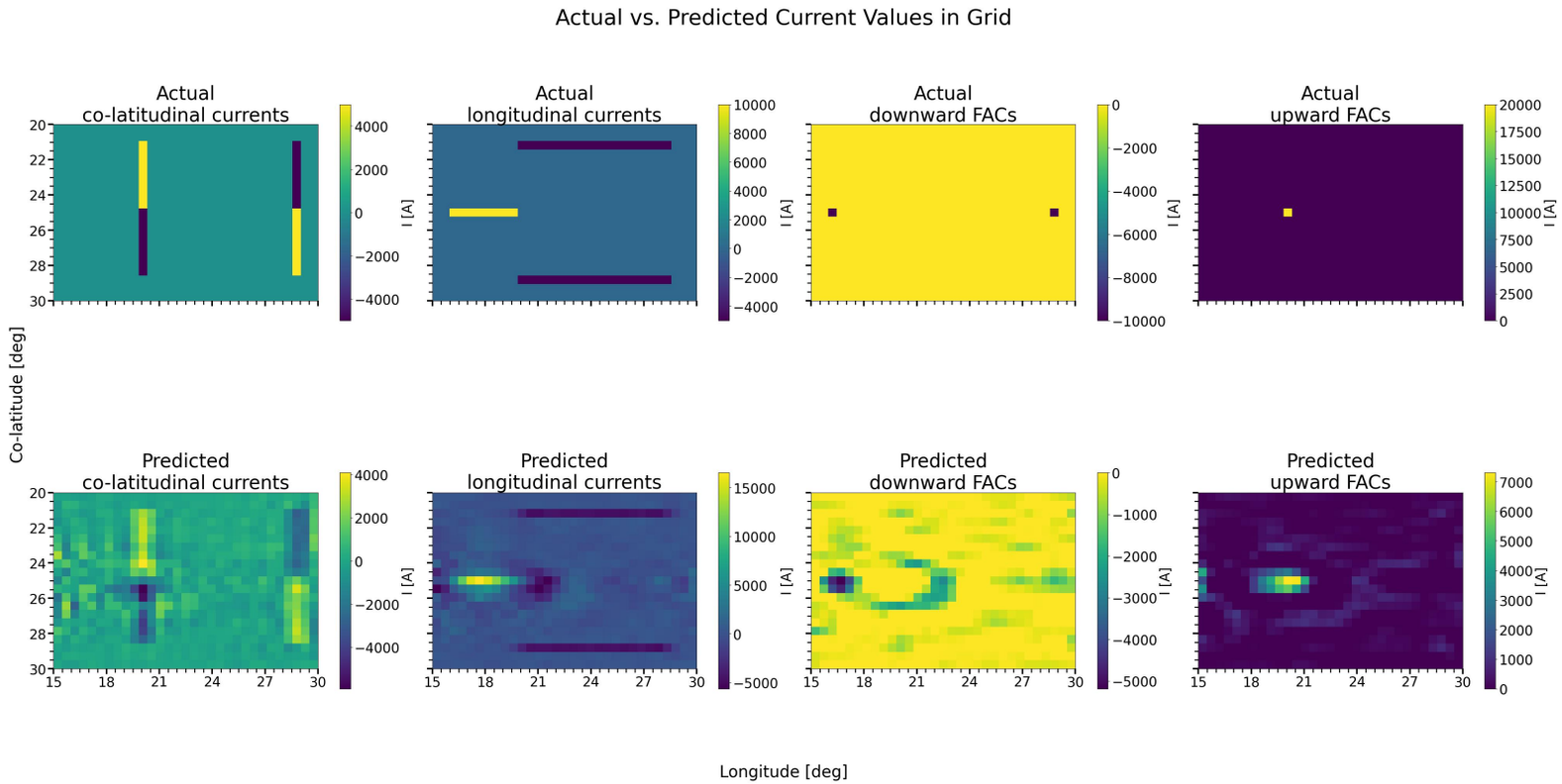

Figure 4.28: The actual (top) and estimated (bottom) co-latitudinal current(left), longitudinal current (center left), downward FAC (center right) and upward FAC (right) grid values for a current system of a set of northward, southward, westward and eastward currents and upward and downward FACs. At (25°co-lat., 29°long.) a 10kA downward FAC comes in and diverges north and south at 5000A each, both travelling 4° and then travelling 9° west before moving towards eachother by 4° again and converging at (25°co-lat., 20°long.). A second 10kA downward FAC comes in at (25°co-lat., 16°long.) and travels east 4° merging with the other currents at (25°co-lat., 20°long.) and travelling as an 20000A upward FAC. The estimated co-latitudinal values have a reduced resolution in the longitudinal direction, while also reduced in magnitude at the easternmost part of the system. The estimated longitudinal values are relatively accurate to the actual system, with some erroneous negative values around the upward FAC and the westernmost downward FAC. The estimated FACs have a reduced resolution in both co-latitudinal and longitudinal directions while also being reduced in magnitude compared to the actual values, with the easternmost downward FAC being the most significantly reduced.

4.3 Results for 100 magnetometer stations

In this section visuals will only be shown for the southward current stream and the multidirectional system of currents to not overwhelm the reader with too many figures.

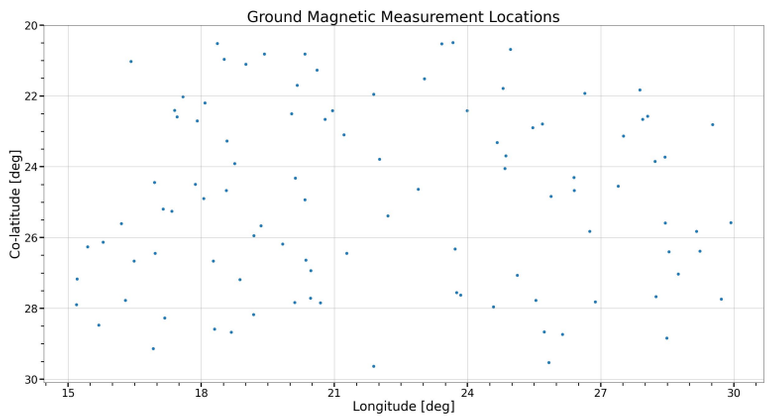

Figure 4.29: 100 randomly distributed ground magnetometer locations within 20° and 30° co-latitude and 15° and 30° longitude.

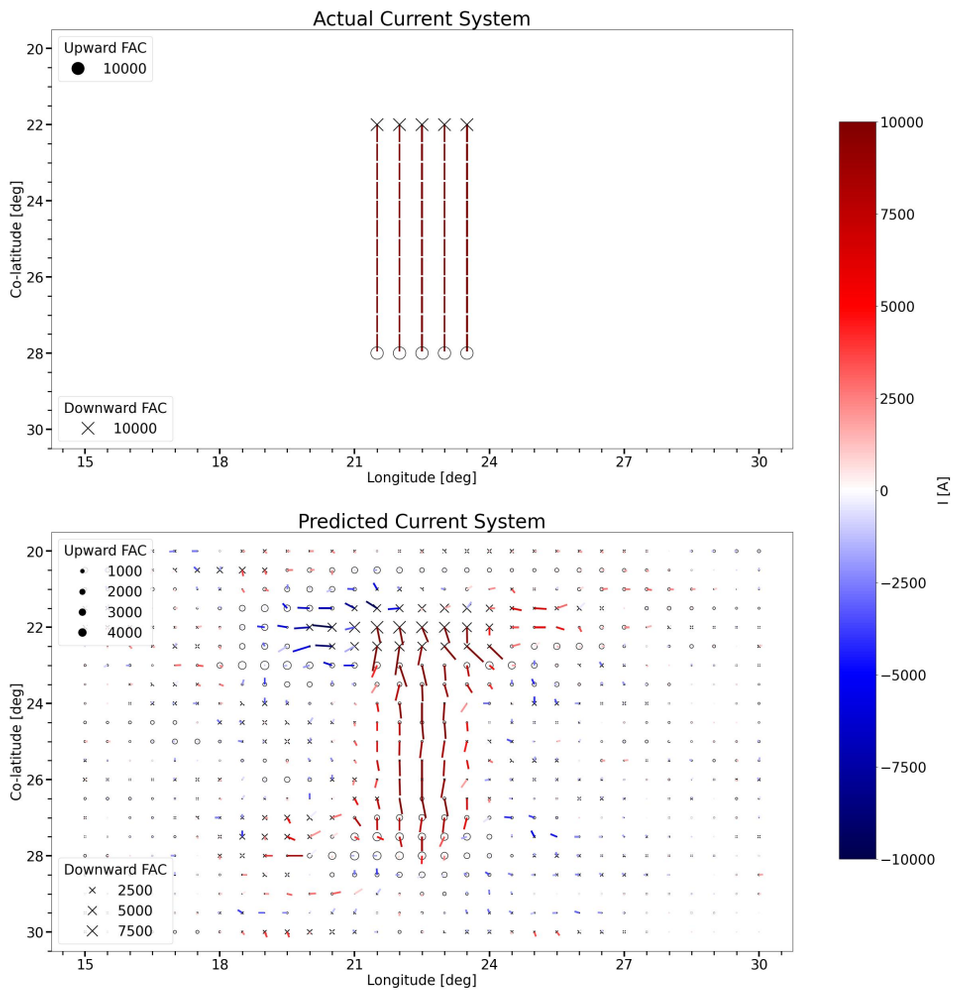

Figure 4.30: Vectorfield of the actual (top) and estimated (bottom) current system of a set of 10kA downward FACs coming in at (22°co-lat., 21.5° – 23.5°long.) and travelling south 6° before travelling as upward FACs at (28°co-lat., 21.5° – 23.5°long.). The estimated horizontal current system are only accurate in the middlemost single current compared to the actual currents, becoming less accurate at the co-latitudinal edges of the current system and along the longitudinal edges. Converging currents surround the south edge and diverging currents surround the north edge of the system, while the southgoing currents along the eastern and western edges have reduced amplitude. The estimated FACs at the edges are reduced in amplitude compared to the actual FACs, with the upward FACs at the south edge being reduced the most. The estimated system has a mean absolute error of $6.74 \cdot 10^{-2}$.

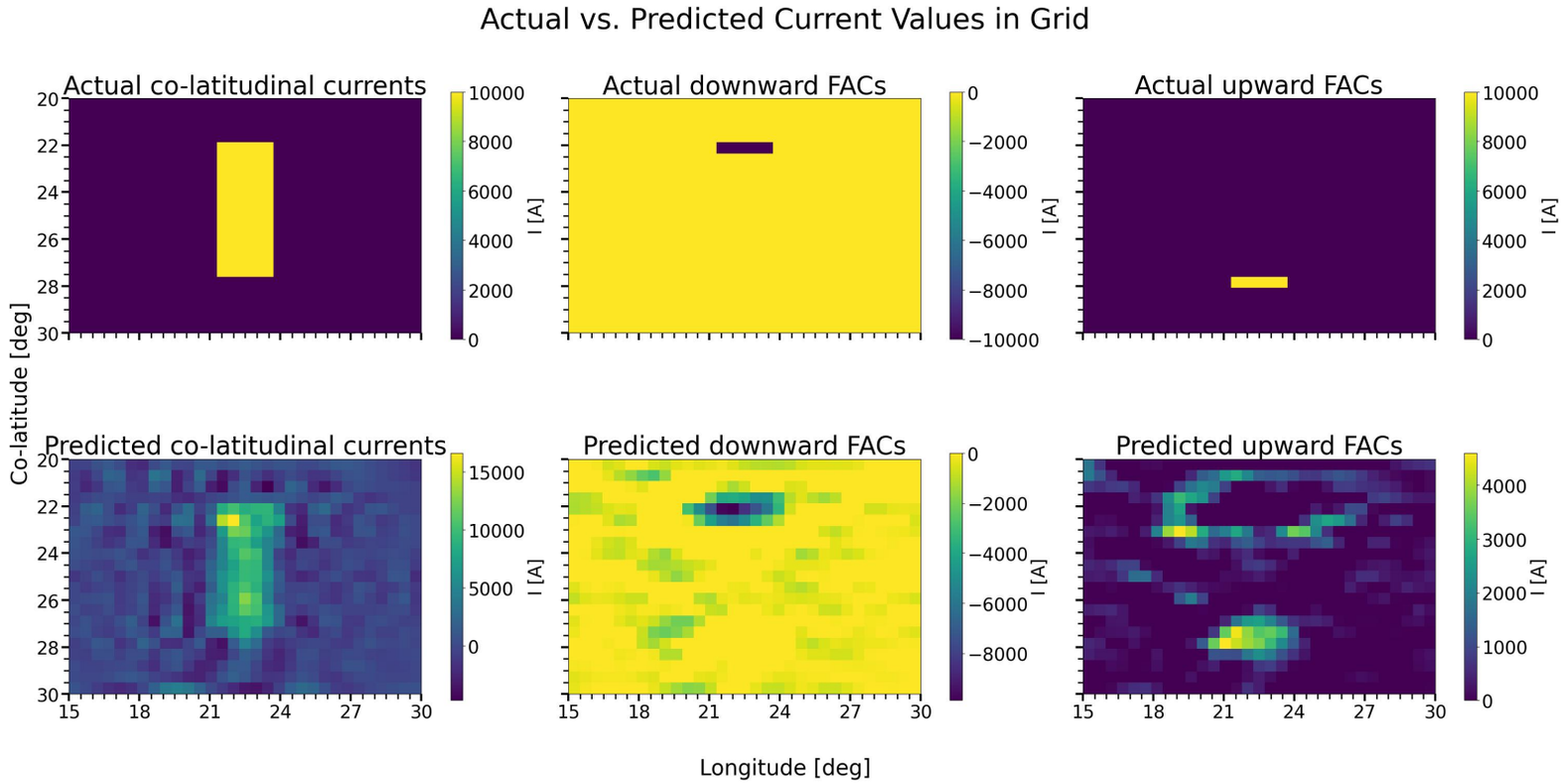

Figure 4.31: The actual (top) and estimated (bottom) longitudinal current (left), downward FAC (center) and upward FAC (right) grid values for a current system of a set of 10kA downward FACs coming in at (22°co-lat., 21.5° – 23.5°long.) and travelling south 6° before travelling as upward FACs at (28°co-lat., 21.5° – 23.5°long.). The estimated co-latitudinal values are reduced along the western and eastern edges compared to the actual values. The estimated upward FAC values are slightly reduced compared to the actual values and has some loss in resolution. The estimated downward FAC values are less accurate in both magnitude and resolution compared to the actual values and a ring of downward FAC values surround the north edge of the system.

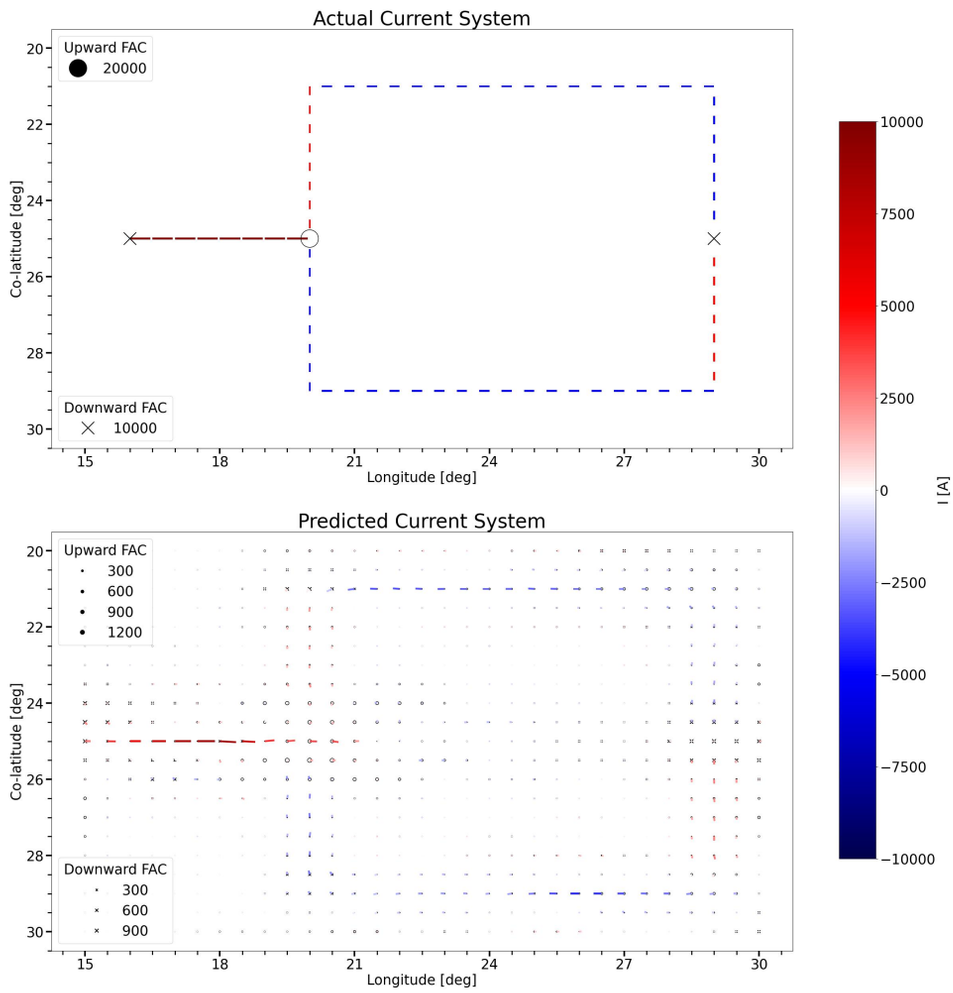

Figure 4.32: Vectorfield of the actual (top) and estimated (bottom) current system of a set of northward, southward, westward and eastward currents and upward and downward FACs. At (25°co-lat., 29°long.) a 10kA downward FAC comes in and diverges north and south at 5000A each, both travelling 4° and then travelling 9° west before moving towards eachother by 4° again and converging at (25°co-lat., 20°long.). A second 10kA downward FAC comes in at (25°co-lat., 16°long.) and travels east 4° merging with the other currents at (25°co-lat., 20°long.) and travelling as an 20000A upward FAC. The estimated system has a low accuracy over the whole system compared to the actual currents. The estimated system has a mean absolute error of $2.56 \cdot 10^{-2}$.

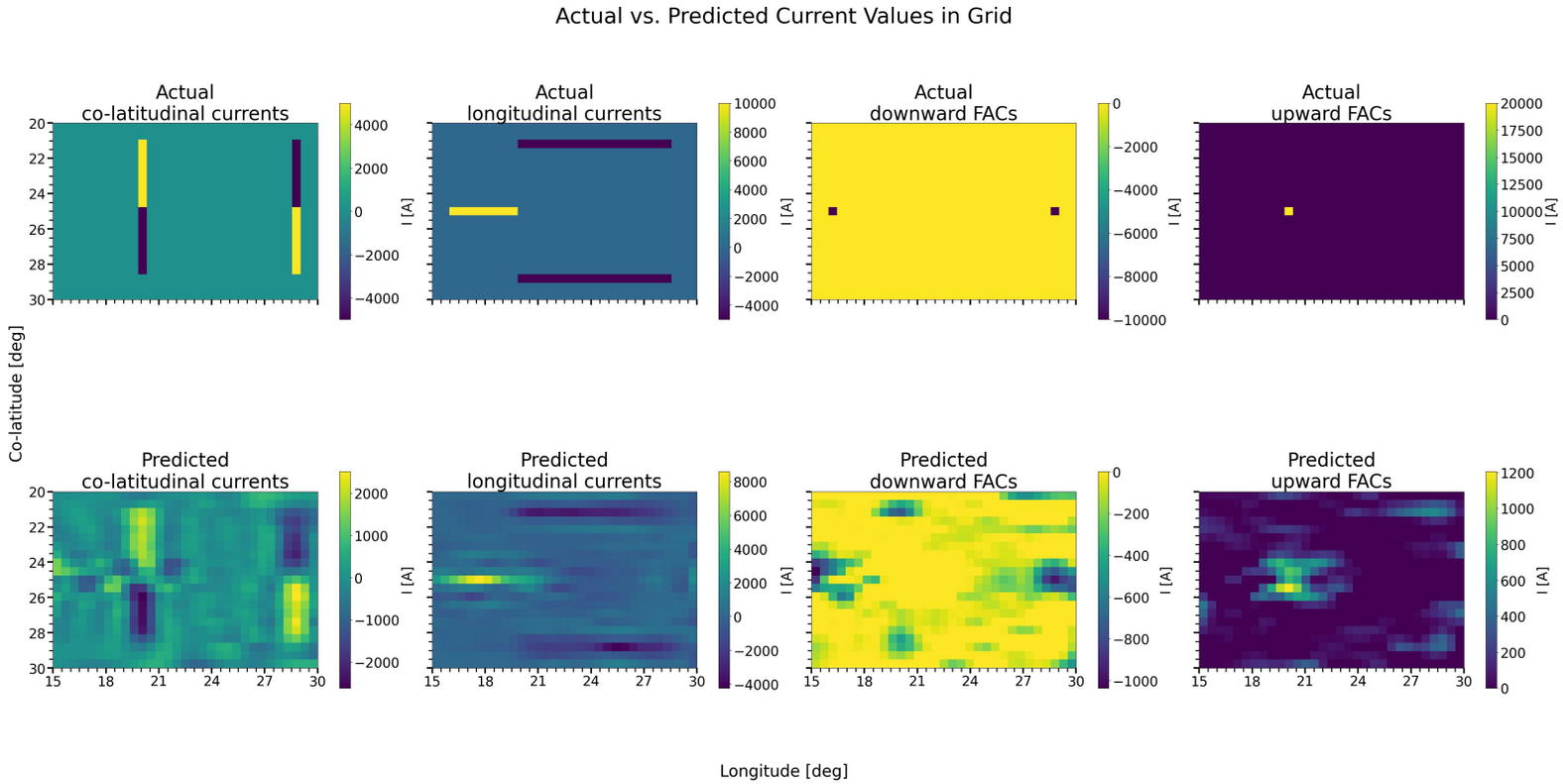

Figure 4.33: The actual (top) and estimated (bottom) co-latitudinal current(left), longitudinal current (center left), downward FAC (center right) and upward FAC (right) grid values for a current system of a set of northward, southward, westward and eastward currents and upward and downward FACs. At (25°co-lat., 29°long.) a 10kA downward FAC comes in and diverges north and south at 5000A each, both travelling 4° and then travelling 9° west before moving towards eachother by 4° again and converging at (25°co-lat., 20°long.). A second 10kA downward FAC comes in at (25°co-lat., 16°long.) and travels east 4° merging with the other currents at (25°co-lat., 20°long.) and travelling as an 20000A upward FAC. The estimated values in all directions have a low accuracy compared to the actual values, with a significant loss in resolution and magnitude.

4.4 Results for 50 magnetometer stations

In this section visuals will only be shown for the southward current stream and the multidirectional system of currents to not overwhelm the reader with too many figures.

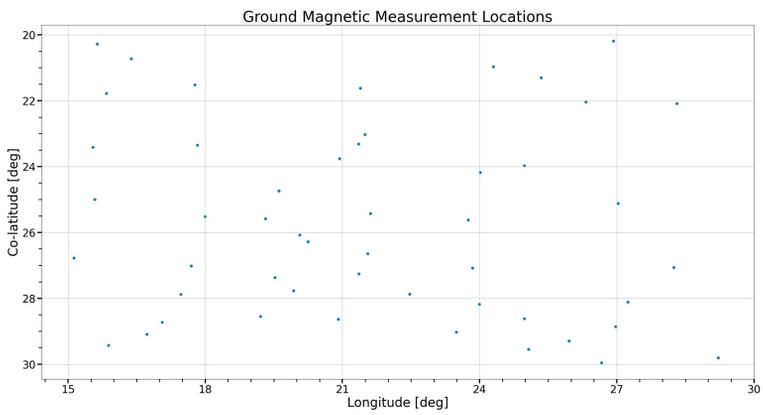

Figure 4.34: 50 randomly distributed ground magnetometer locations within 20° and 30° co-latitude and 15° and 30° longitude.

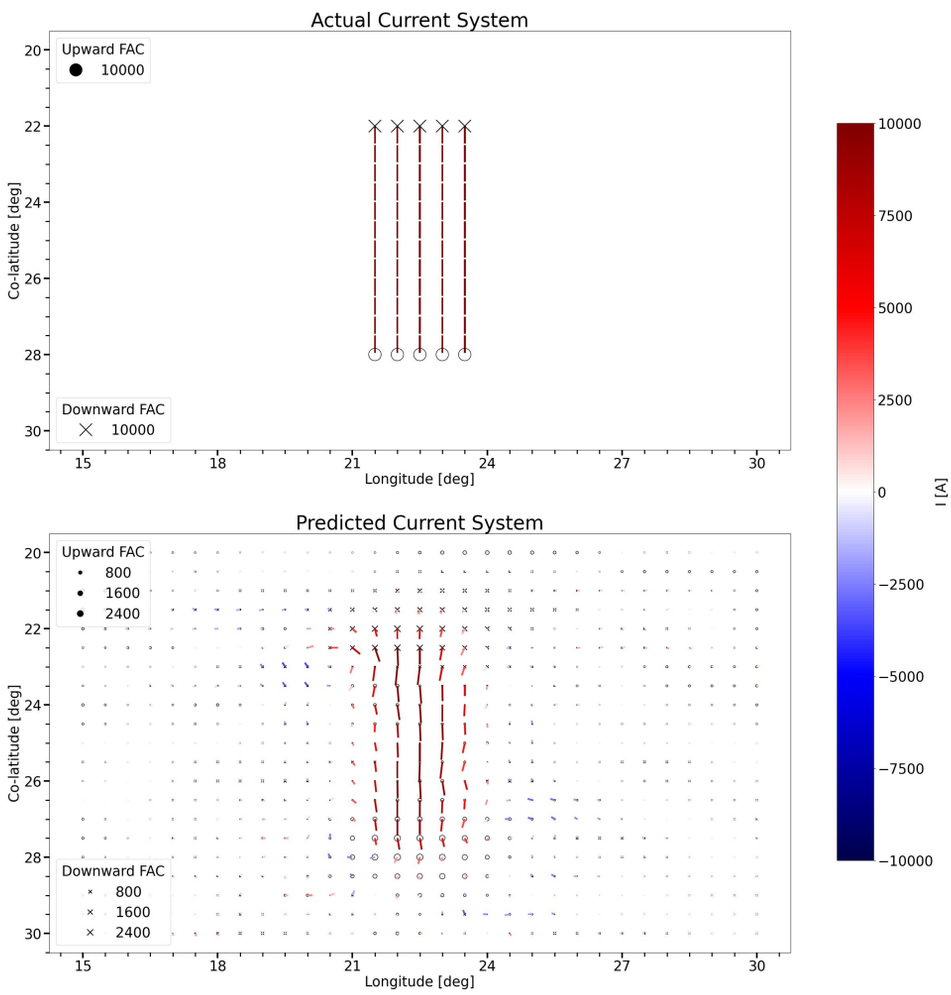

Figure 4.35: Vectorfield of the actual (top) and estimated (bottom) current system of a set of 10kA downward FACs coming in at (22°co-lat., 21.5° – 23.5°long.) and travelling south 6° before travelling as upward FACs at (28°co-lat., 21.5° – 23.5°long.). The estimated horizontal current system are relatively accurate in the middle of the current system compared to the actual currents, but becomes less accurate at edges of the current system where it has reduced amplitude. The estimated FACs have low accuracy compared to the actual FACs with a significant reduction in amplitude. The estimated system has a mean absolute error of $2.16 \cdot 10^{-1}$.

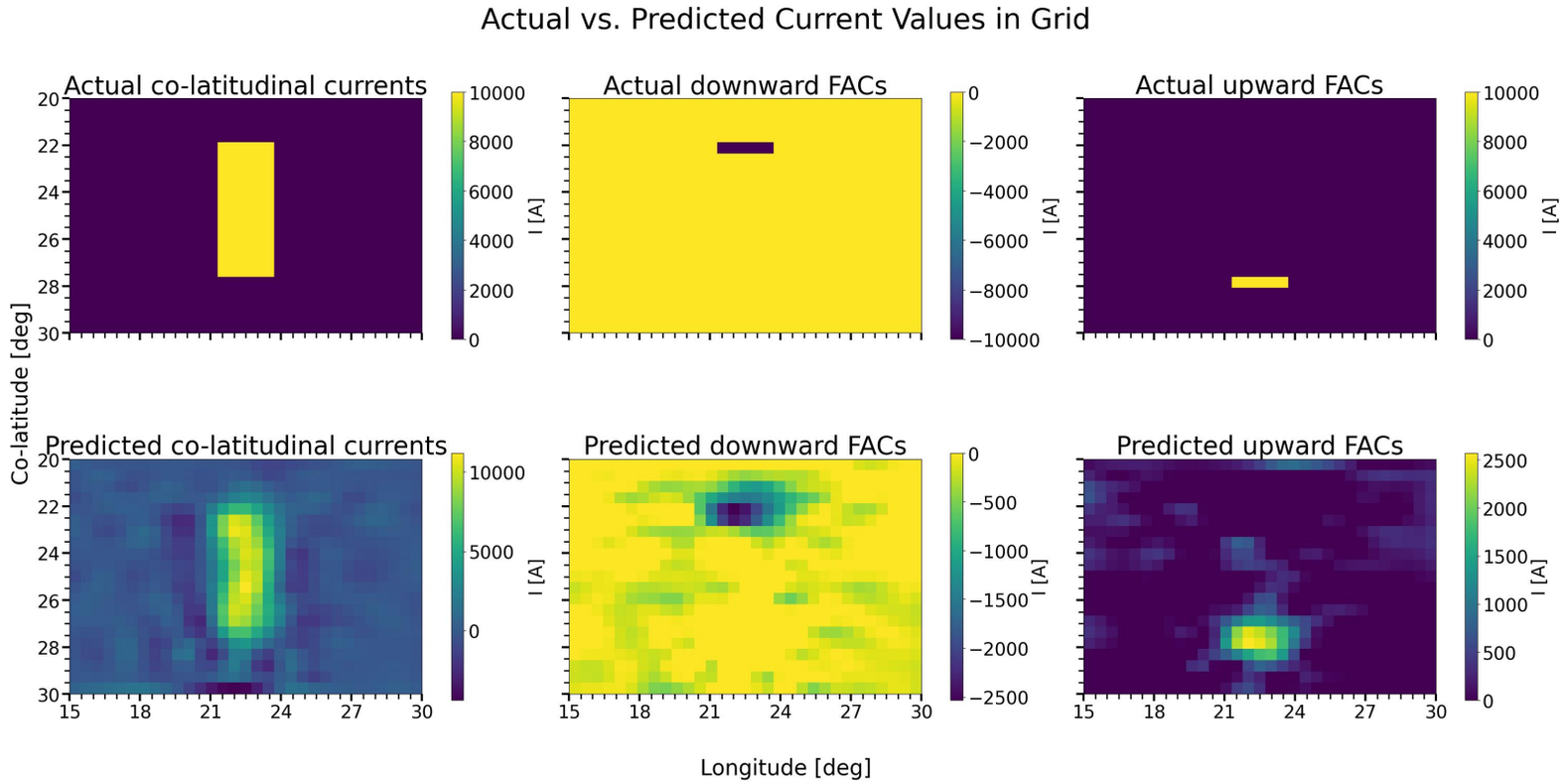

Figure 4.36: The actual (top) and estimated (bottom) longitudinal current (left), downward FAC (center) and upward FAC (right) grid values for a current system of a set of 10kA downward FACs coming in at (22°co-lat., 21.5° – 23.5°long.) and travelling south 6° before travelling as upward FACs at (28°co-lat., 21.5° – 23.5°long.). The estimated co-latitudinal values coincide with the actual values in the middle of the current system, but are overestimated around the north edge and underestimated around the south edge of the current system. The estimated FAC values are relatively accurate to the actual values, but with some loss in resolution and some noisy rings of opposite low magnitude FAC values surrounding them.

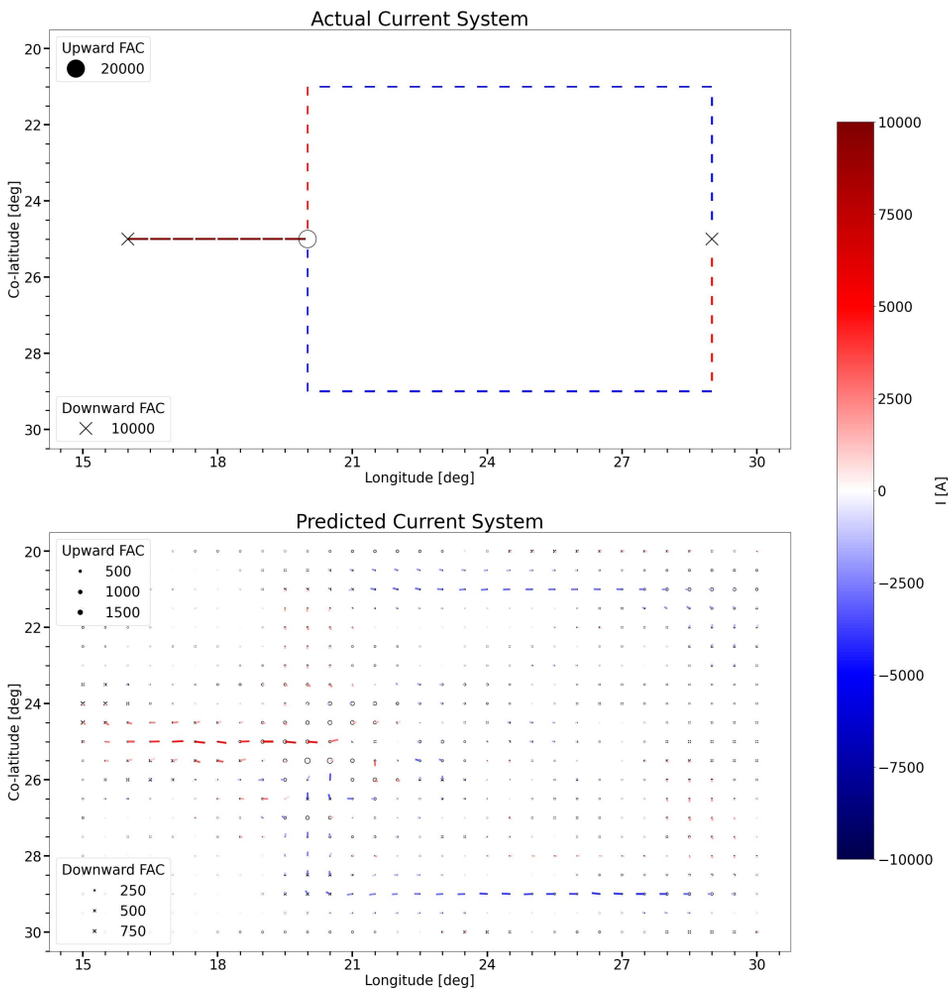

Figure 4.37: Vectorfield of the actual (top) and estimated (bottom) current system of a set of northward, southward, westward and eastward currents and upward and downward FACs. At (25°co-lat., 29°long.) a 10kA downward FAC comes in and diverges north and south at 5000A each, both travelling 4° and then travelling 9° west before moving towards eachother by 4° again and converging at (25°co-lat., 20°long.). A second 10kA downward FAC comes in at (25°co-lat., 16°long.) and travels east 4° merging with the other currents at (25°co-lat., 20°long.) and travelling as an 20000A upward FAC. The estimated system has relatively accurate longitudinal currents compared to the actual current system, but poor accuracy for the co-latitudinal currents. The estimated FACs vary in accuracy with the westernmost downward FAC and the upward FAC more accurately estimated than the easternmost downward FAC. The estimated system has a mean absolute error of $2.35 \cdot 10^{-2}$.

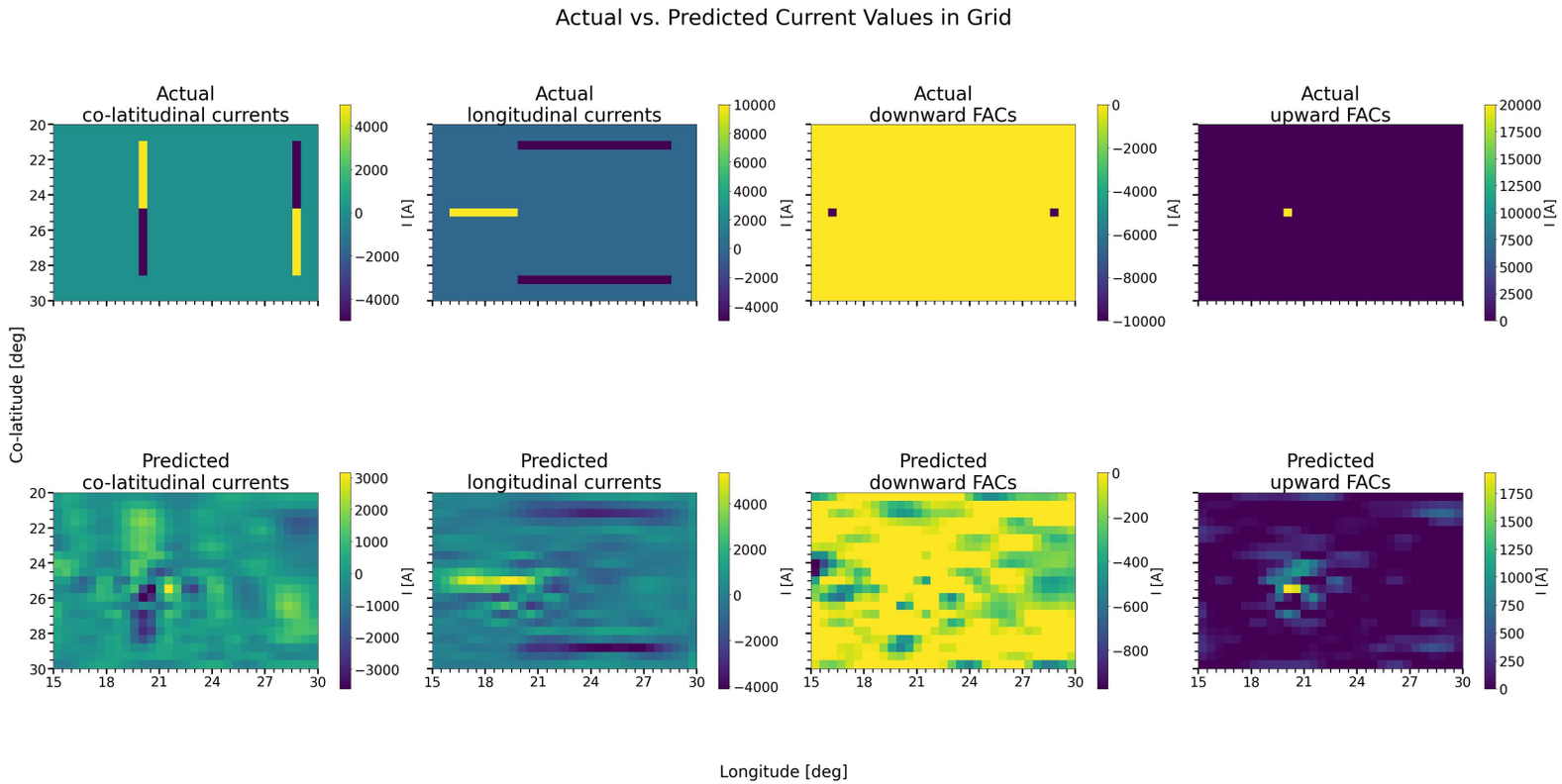

Figure 4.38: The actual (top) and estimated (bottom) co-latitudinal current(left), longitudinal current (center left), downward FAC (center right) and upward FAC (right) grid values for a current system of a set of northward, southward, westward and eastward currents and upward and downward FACs. At (25°co-lat., 29°long.) a 10kA downward FAC comes in and diverges north and south at 5000A each, both travelling 4° and then travelling 9° west before moving towards eachother by 4° again and converging at (25°co-lat., 20°long.). A second 10kA downward FAC comes in at (25°co-lat., 16°long.) and travels east 4° merging with the other currents at (25°co-lat., 20°long.) and travelling as an 20000A upward FAC. The estimated co-latitudinal values have a reduced resolution in the longitudinal direction, while also reduced in magnitude at the easternmost part of the system. The estimated longitudinal values are relatively accurate to the actual system, with some erroneous negative values around the upward FAC and the westernmost downward FAC. The estimated FACs have a reduced resolution in both co-latitudinal and longitudinal directions while also being reduced in magnitude compared to the actual values, with the easternmost downward FAC being the most significantly reduced.

5

Summary and conclusion

A method based off standard linear inverse problem methods was developed. A Tikhonov regularization utilizing current continuity laws was used to obtain physically sensible current solutions on a simple ionospheric wireframe model from ground-based magnetic field observations from a set of artificial current systems. The model test results indicate that isolated FACs might be able to get resolved if they are separated by a couple of degrees when working in the auroral region.

5.1 Future work

As this thesis is the initial development of the new estimation method using the GICi3D model it is difficult to determine where the method development is headed. It was tested in this thesis in very ideal conditions with generally accurate estimations for simple current systems and less accurate estimations for more complex systems. If the method has potential to work in estimating real ionospheric current systems depends on further development and testing.

Bibliography

P. Alken, E. Thébault, C. Beggan, H. Amit, J. Aubert, J. Baerenzung, T. Bondar, W. Brown, S. Califf, A. Chambodut, et al. Matching entries: o settings... *Earth, Planets and Space*, 73(1):49, 2021.

J. Allen, H. Sauer, L. Frank, and P. Reiff. Effects of the march 1989 solar activity. *Eos, Transactions American Geophysical Union*, 70(46):1479–1488, 1989.

O. Amm. Ionospheric elementary current systems in spherical coordinates and their application. *Journal of geomagnetism and geoelectricity*, 49(7):947–955, 1997. doi: 10.5636/jgg.49.947.

O. Amm and A. Viljanen. Ionospheric disturbance magnetic field continuation from the ground to the ionosphere using spherical elementary current systems. *Earth, Planets and Space*, 51(6):431–440, 1999. doi: 10.1186/BF03352247.

R. C. Aster, B. Borchers, and C. H. Thurber. Chapter two - linear regression. In R. C. Aster, B. Borchers, and C. H. Thurber, editors, *Parameter Estimation and Inverse Problems (Third Edition)*, pages 25–53. Elsevier, third edition edition, 2019a. ISBN 978-0-12-804651-7. doi: https://doi.org/10.1016/B978-0-12-804651-7.00007-9. URL https://www.sciencedirect.com/science/article/pii/B9780128046517000079.

R. C. Aster, B. Borchers, and C. H. Thurber. Chapter four - tikhonov regularization. In R. C. Aster, B. Borchers, and C. H. Thurber, editors, *Parameter Estimation and Inverse Problems (Third Edition)*, pages 93–134. Elsevier, third edition edition, 2019b. ISBN 978-0-12-804651-7. doi: https://doi.org/10.1016/B978-0-12-804651-7.00009-2. URL https://www.sciencedirect.com/science/article/pii/B9780128046517000092.

A. Brekke. *Physics of the Upper Polar Atmosphere*. Springer Atmospheric Sciences. Springer Berlin Heidelberg, 2012. ISBN 9783642274015. URL https://books.google.no/books?id=fRVLAAAAQBAJ.

J. W. Dungey. Interplanetary magnetic field and the auroral zones. *Phys. Rev. Lett.*, 6:47–48, Jan 1961. doi: 10.1103/PhysRevLett.6.47. URL https://link.aps.org/doi/10.1103/PhysRevLett.6.47.

J. Elfritz. Ion temperatures in earth's inner magnetosphere: Ring current dynamics, transient effects, and data-model comparisons. 2014.

N. Fukushima. Generalized theorem for no ground magnetic effect of vertical currents connected with pedersen currents in the uniform-conductivity ionosphere. *REP. IONOSPH. SPACE RES. JAP.; JAP.; DA. 1976; VOL. 30; NO 1-2; PP. 35-40; BIBL. 6 REF.*, 1976.

M. Hesse and P. A. Cassak. Magnetic reconnection in the space sciences: Past, present, and future. *Journal of Geophysical Research: Space Physics*, 125(2):e2018JA025935, 2020. doi: https://doi.org/10.1029/2018JA025935. URL https://agupubs.onlinelibrary.wiley.com/doi/abs/10.1029/2018JA025935. e2018JA025935 2018JA025935.

K. M. Laundal, S. E. Haaland, N. Lehtinen, J. W. Gjerloev, N. Østgaard, P. Tenfjord, J. P. Reistad, K. Snekvik, S. E. Milan, S. Ohtani, and B. J. Anderson. Birkeland current effects on high-latitude ground magnetic field perturbations. *Geophysical Research Letters*, 42(18):7248–7254, 2015. doi: https://doi.org/10.1002/2015GL065776. URL https://agupubs.onlinelibrary.wiley.com/doi/abs/10.1002/2015GL065776.

S. Milan, L. Clausen, J. Coxon, J. Carter, M.-T. Walach, K. M. Laundal, N. Østgaard, P. Tenfjord, J. Reistad, K. Snekvik, and B. Anderson. Overview of solar wind–magnetosphere–ionosphere–atmosphere coupling and the generation of magnetospheric currents. *Space Science Reviews*, 206, 03 2017. doi: 10.1007/s11214-017-0333-0.

P. T. Newell and J. W. Gjerloev. Local geomagnetic indices and the prediction of auroral power. *Journal of Geophysical Research: Space Physics*, 119(12): 9790–9803, 2014.

A. D. Richmond. *Ionosphere*, pages 452–454. Springer Netherlands, Dordrecht, 2007. ISBN 978-1-4020-4423-6. doi: 10.1007/978-1-4020-4423-6_159. URL https://doi.org/10.1007/978-1-4020-4423-6_159.

R. M. Robinson, R. R. Vondrak, K. Miller, T. Dabbs, and D. Hardy. On calculating ionospheric conductances from the flux and energy of precipitating electrons. *Journal of Geophysical Research: Space Physics*, 92(A3):2565–2569, 1987. doi: https://doi.org/10.1029/JA092iA03p02565. URL https://agupubs.onlinelibrary.wiley.com/doi/abs/10.1029/JA092iA03p02565.

R. Schunk and A. Nagy. *Ionospheres: physics, plasma physics, and chemistry*. Cambridge university press, 2009.

K. Seki, A. Nagy, C. Jackman, F. Crary, D. Fontaine, P. Zarka, P. Wurz, A. Milillo, J. Slavin, D. Delcourt, M. Wiltberger, R. Ilie, X. Jia, S. Ledvina, M. Liemohn, and R. Schunk. A review of general physical and chemical processes related to plasma sources and losses for solar system magnetospheres. *Space Science Reviews*, 192, 08 2015. doi: 10.1007/s11214-015-0170-y.

J. Untiedt and u. W. Baumjohann. Studies of polar current systems using the ims scandinavian magnetometer array. *Space Science Reviews*, 63(3):245–390, 1993.

V. M. Vasyliūnas. The physical basis of ionospheric electrodynamics. *Annales Geophysicae*, 30(2):357–369, 2012. doi: 10.5194/angeo-30-357-2012. URL `https://angeo.copernicus.org/articles/30/357/2012/`.

E. Z. W. Lyatsky, S. Lyatskaya. Effect of interhemispheric currents on equivalent ionospheric currents in two hemispheres: Simulation results. *Journal of Geophysical Research: Space Physics*, 121, 2015. doi: https://doi.org/10.1002/2015JA021167.

Y. Wang. Introduction. In *Magnetic Cloud Boundary Layers and Magnetic Reconnection*, pages 1–21. Springer, 2015.